

# Galaxy-galaxy weak lensing in SDSS: intrinsic alignments and shear calibration errors

Christopher M. Hirata<sup>1?</sup>, Rachel Mandelbaum<sup>1</sup>, Uros Seljak<sup>1</sup>,  
 Jacek Guzik<sup>2</sup>, Nikhil Padmini Anabhan<sup>1</sup>, Cullen Blake<sup>3</sup>, Jonathan Brinkmann<sup>4</sup>,  
 Tamás Budavári<sup>5</sup>, Andrew Connolly<sup>6</sup>, István Csabai<sup>7</sup>, Ryan Scranton<sup>6</sup>,  
 and Alexander S. Szalay<sup>5</sup>

<sup>1</sup>Department of Physics, Jadwin Hall, Princeton University, Princeton NJ 08544, USA

<sup>2</sup>Astronomical Observatory, Jagiellonian University, Orla 171, 30-244 Krakow, Poland

<sup>3</sup>Princeton Observatory, Princeton University, Princeton NJ 08544, USA

<sup>4</sup>Apache Point Observatory, 2001 Apache Point Road, Sunspot NM 88349-0059, USA

<sup>5</sup>Department of Physics and Astronomy, Johns Hopkins University, 3701 San Martin Drive, Baltimore MD 21218, USA

<sup>6</sup>University of Pittsburgh, Department of Physics and Astronomy, 3941 O'Hara Street, Pittsburgh PA 15260, USA

<sup>7</sup>Department of Physics, Eötvos University, Budapest, P. f. 32, Hungary, H-1518

22 May 2019

## ABSTRACT

Galaxy-galaxy lensing has emerged as a powerful probe of the dark matter halos of galaxies, but is subject to contamination if intrinsically aligned satellites of the lens galaxy are used as part of the source sample. We present a measurement of this intrinsic shear using 200,747 lens galaxies from the Sloan Digital Sky Survey (SDSS) spectroscopic sample and a sample of satellites selected using photometric redshifts. The mean intrinsic shear at transverse separations of  $30\{446h^{-1}$  kpc is constrained to be  $0.0062 < \gamma < +0.0066$  (99.9 per cent confidence, including identified systematics), which limits its contamination of the galaxy-galaxy lensing signal to at most 15 per cent on these scales. We present these limits as a function of transverse separation and lens luminosity. We furthermore investigate shear calibration biases in the SDSS and conclude that the shear amplitude is calibrated to better than 18 per cent. This includes noise-induced calibration biases in the ellipticity, which are small for the sample considered here, but which can be more important if low signal-to-noise or poorly resolved source galaxies are used.

**Key words:** galaxies: halos { gravitational lensing.

## 1 INTRODUCTION

Weak gravitational lensing has emerged as a powerful tool for directly measuring the matter distribution in the universe (e.g. Bartelmann & Schneider 2001; Refregier 2003). One of its applications has been the measurement of the projected matter density of galaxies (Hudson et al. 1998; Fischer et al. 2000; Smith et al. 2001; McKinley et al. 2001; Guzik & Seljak 2002; Sheldon et al. 2003), groups, and clusters (Hoekstra et al. 2001; Hoekstra et al. 1998; Sheldon et al. 2001). In these measurements, the observable quantity is the tangential shear  $\gamma_t$  of distant source galaxies induced by the lens. It is however possible that some of the "source" galaxies whose shears are used to measure lensing may in fact be physically associated with the lens;

in this case they may be intrinsically aligned with the lens, producing a false lensing signal. This false signal may be quantified by the "intrinsic shear"  $\gamma_i$ , which is the spurious estimate of the tangential shear that would be obtained by applying a shear estimator to a population of physically associated galaxies (see Appendix A for a more precise definition). This intrinsic shear is essentially a type of galaxy density-shear correlation, i.e. it measures the correlation between the shears of some galaxies and the positions of others; it is distinct from the shear-shear correlations that contaminate the gravitational shear autocorrelation measured by lensing surveys in the field (Van Waerbeke et al. 2000; Bacon et al. 2000; Rhodes et al. 2001; Hoekstra et al. 2002; Van Waerbeke et al. 2002; Jarvis et al. 2003; Brown et al. 2003).

Several investigators have investigated this potential contaminant of the lensing signal. Lee & Pen (2001) mea-

? Electronic address: chirata@princeton.edu

sured the density-shear correlation using 12,122 spiral galaxies. These authors were primarily interested in the rotation axes of galaxies and their possible use as tracers of the large-scale tidal field (and hence the cosmic density perturbations; Lee & Pen 2000), and so they measure position angles rather than shear. A crude (and model-dependent) conversion of their measurements into an intrinsic shear suggests

$$\gamma = 0.0037 \pm 0.0025 \text{ at separations } r_D = 500h^{-1} \text{ kpc} \quad (\text{see Appendix B}).$$

Bernstein & Norberg (2002) used 1,819 satellite galaxies selected spectroscopically from the Two-Degree Field (2dF) Galaxy Redshift Survey (Colless et al. 2001) with ellipticities measured in the Automatized Plate Measuring (APM) survey (Maddox et al. 1990) to set an upper limit on the intrinsic shear of the satellite galaxies of  $\langle |\gamma| \rangle \approx 0.01$  (at 95 per cent confidence)<sup>1</sup> for primary-satellite pairs separated by a transverse distance of  $< 350h^{-1}$  kpc. However, this upper limit is not presented as a function of transverse separation or lens luminosity. Circularization of the galaxy images due to the APM point-spread function (PSF) may weaken the upper limit slightly (by 10–20 per cent; Bernstein & Norberg 2002) but this does not alter the conclusion that intrinsic alignment contamination of the galaxy-galaxy lensing signal observed by Fischer et al. (2000) and McKay et al. (2001) is limited to 20 per cent.

There have been other observational studies of intrinsic alignments, including reported detections of higher-order density-shear statistics (Lee & Pen 2002) and shear-shear correlations (Pen et al. 2000; Brown et al. 2002); unfortunately there is no simple conversion from these measurements into an intrinsic shear.

Theoretical work on galaxy intrinsic alignments has been motivated both by inherent interest and (more recently) by contamination of cosmic shear surveys for which the intrinsic-alignment parameter of interest is the shear-shear correlation instead of the density-shear correlation. A number of estimates of the shear-shear correlations (both in N-body simulations and in analytical models) have been made (Croft & Metzler 2000; Heavens et al. 2000; Lee & Pen 2000; Lee & Pen 2001; Cattaneo et al. 2001; Crittenden et al. 2001; Jing 2002). Usually the galaxy is approximated as a disk aligned perpendicular to the halo angular momentum vector (for spirals) or as an ellipsoid homologous with the ellipticity of its halo (for ellipticals), although comparison to observations (Heymans et al. 2004) and simulations of galaxy formation (Van den Bosch et al. 2002) suggest that this picture is too simple and overestimates the shear-shear correlations. Of these authors, only Lee & Pen (2001) estimate the density-shear correlation (and even then only for spirals). Using the rough conversion of Appendix B, their prediction corresponds to  $\gamma = 0.004$  for the spiral sources, the sign indicating radial alignment.

In this paper, we use SDSS spectroscopic galaxies (as lenses) and photometric galaxies (as sources) in a luminosity-dependent study of the shear around lens galaxies due to intrinsic alignments. The large number of galaxies in the SDSS photometric sample allows tighter constraints on  $\gamma$  than were obtained by Bernstein & Norberg (2002).

<sup>1</sup> Bernstein & Norberg (2002) reported an upper limit on the ellipticity of 0.02, which we have converted here to a shear.

It also provides the statistical power to compute these upper limits as a function of transverse separation and lens luminosity. To make the interpretation for weak lensing as simple as possible, we directly compute  $\gamma$  using a lensing estimator (including PSF corrections) rather than the position-angle statistics of Lee & Pen (2001) or the unweighted moments computed by the APM survey.

Correct calibration of the shear estimator is necessary in order to interpret either an intrinsic alignment or a weak lensing-induced shear. Errors in shear calibration can come from a variety of effects such as incomplete PSF correction, selection effects, noise-induced biases, uncertainties in PSF reconstruction, and incomplete knowledge of the ellipticity distribution of the source population (Kaiser 2000; Bernstein & Jarvis 2002; Hirata & Seljak 2003). Since we do not detect an intrinsic alignment signal, the only effect of calibration uncertainty is a minor degradation of our upper limits on  $\gamma$ . Nevertheless, the calibration results presented here should be of direct interest for ongoing galaxy-galaxy weak lensing studies with the SDSS. The noise-induced calibration biases have not been explicitly studied previously; while we find that this effect is insignificant for our sample of relatively bright ( $r < 21$ ) galaxies, the calibration bias can be large for galaxies detected at low signal-to-noise ratio, especially if they are also not well-resolved.

This paper is organized as follows: Sec. 2 includes a description of the lens catalog, and Sec. 3 includes discussion of the source catalog, including details of the apparent shear measurement, the associated calibration uncertainties, and the photometric redshifts. In Sec. 4, we describe the methods used to compute uncertainties on the shear. Sec. 5 includes results for intrinsic and gravitational shear, and the results of tests for systematic errors affecting these quantities. We conclude in Sec. 6 with a discussion of the implications of these results. The noise-induced calibration bias derivation is presented in Appendix C.

A note about the cosmological model and units used in this paper: we compute the proper transverse separation of the lens and source using the physical angular diameter distance  $d_A(z_1)$  to the lens. This distance is determined assuming a flat CDM universe with  $\Omega_m = 0.27$  and  $\Omega_b = 0.73$ , in accord with cosmological parameter determinations from the Wilkinson Microwave Anisotropy Probe (Spergel et al. 2003). We present distances in  $h^{-1}$  kpc, where  $h$  is the reduced Hubble parameter:  $H_0 = 100h \text{ km/s/Mpc}$ . When appropriately scaled by  $h$ , the angular diameter distance is only weakly sensitive even to extreme variations in cosmology: for a lens at redshift  $z = 0.3$  (among the most distant in our sample; see Fig. 2), we find that  $d_A(z_1)$  is reduced by 7 per cent if we switch from CDM to an open universe ( $\Omega_m = 0.27$ ,  $\Omega_b = 0$ ), and by 12 per cent if we switch to an Einstein-de Sitter universe ( $\Omega_m = 1$ ,  $\Omega_b = 0$ ). Given that we see no detection of intrinsic alignments, the dependence of our results on  $\Omega_m$  and  $\Omega_b$  is negligible for the purpose of constraining contamination of the weak lensing signal.

## 2 LENS CATALOG

The "lenses" used in this investigation are obtained from the SDSS main galaxy spectroscopic sample (York et al. 2000; Strauss et al. 2002; Blanton et al. 2003a). Our sample con-

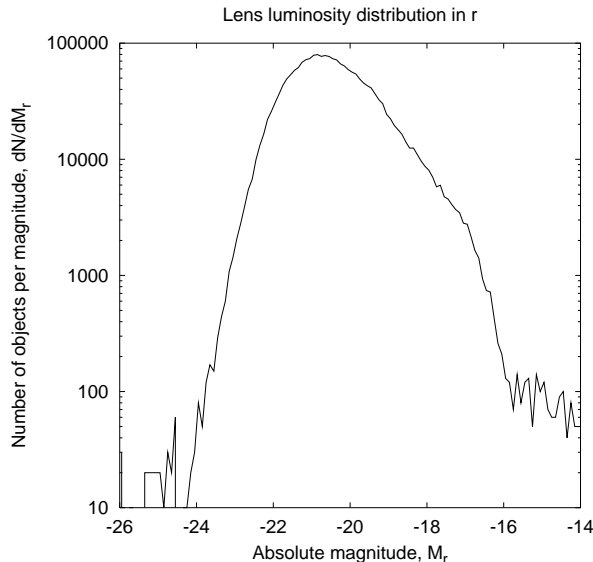


Figure 1. The magnitude distribution of lens galaxies.

tains 200,747 galaxies within a solid angle of 2,499 square degrees (SDSS Sample 12; Blanton et al. 2003a). This sample is approximately flux-limited at Petrosian magnitude  $r < 17.77$  (Strauss et al. 2002). (The  $r$  filter is centered at 622 nm; Fukugita et al. 1996). We have taken only objects at redshift  $z > 0.02$  (at lower redshifts, the summation of pairs of galaxies out to  $1h^{-1} Mpc$  transverse separation becomes computationally expensive, and little is gained anyway because of the small  $\propto$ ). These spectra have been processed by an independent spectroscopic pipeline at Princeton (Schlegel et al. 2004); comparisons with the survey pipeline show that the failures occur < 1 per cent of the time. The objects have been extinction-corrected using the model of Schlegel et al. (1998) extrapolated to the SDSS filters using an extinction-to-reddening ratio  $R_V = 3.1$ , and  $K$ -corrected to  $z = 0.1$  using  $K$ -correct v1.11 (Blanton et al. 2003b).

Fig. 1 shows the magnitude distribution of the lens galaxies, and Fig. 2 shows their redshift distribution, overall and as a function of luminosity. We have used model magnitudes (i.e. magnitudes determined from the best-fit de Vaucouleurs or exponential profile; Stoughton et al. 2002) for both the lens and the source galaxies in this paper.

### 3 SOURCE CATALOG

#### 3.1 Apparent shear measurement

In this section we discuss the methodology for measuring the apparent shear of source galaxies. In general, this must consist of the following steps:

- (i) Source galaxy detection and selection;
- (ii) Point-spread function (PSF) determination;
- (iii) Measurement of galaxy ellipticity, including PSF correction;
- (iv) Conversion of ellipticity measurement into a shear.

If we intend to measure the radial profile of galaxy halos, we must also use redshift and cosmological information to

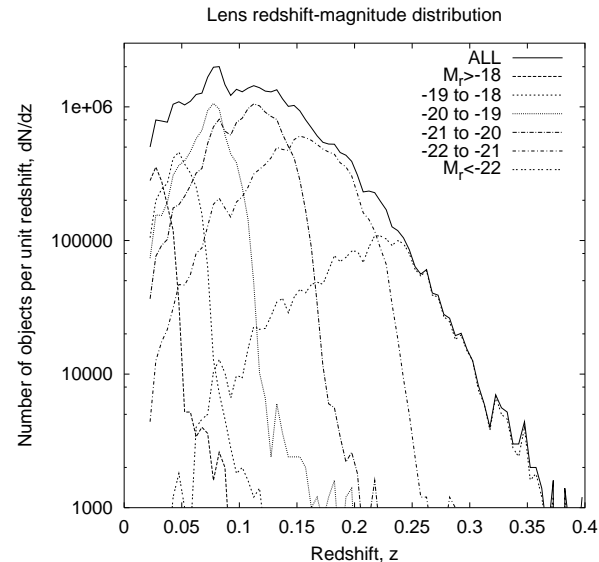


Figure 2. The redshift distribution of lens galaxies, overall and as a function of luminosity. Note that the brighter (smaller  $M_r$ ) subsamples peak at higher redshift.

convert the shear measurements into constraints on the mass distribution. However, in this paper we are only interested in determining the spurious contribution to the apparent shear from intrinsic alignment of source and lens galaxies. Therefore we only work through the four steps outlined above. Also, the reconstruction of the PSF from stellar images is carried out by standard SDSS software (Stoughton et al. 2002; Lupton et al. 2004) and will not be described here.

#### 3.1.1 Adaptive moments

We begin by defining the adaptive moments, which are used in the source selection and ellipticity measurement. The adaptive second moment matrix  $M$  of a galaxy's image intensity  $I(x; y)$  is found by minimizing the energy functional:

$$E(A; x_0, y_0; M; I) = \frac{1}{2} \int \int (I(x; y) - A e^{-\frac{(x-x_0)^2 + (y-y_0)^2}{2}})^2 dx dy, \quad (1)$$

where:

$$e^{-\frac{(x-x_0)^2 + (y-y_0)^2}{2}} = (x - x_0)^T M^{-1} (x - x_0) \quad (2)$$

and  $r = (x; y)$ . The vector  $r_0$  is the object centroid, and the moment matrix  $M$  is taken to be symmetric and can be parameterized as:

$$M = \frac{T}{2} \begin{matrix} 1 + e_+ & e_- \\ e_+ & 1 - e_- \end{matrix} : \quad (3)$$

Here  $T$  is called the trace, and  $e = (e_+; e_-)$  form the spin-2 ellipticity. As defined here the ellipticity is restricted to lie in the unit circle  $e_+^2 + e_-^2 \leq 1$ .<sup>2</sup> The trace is one measure of the "size" of an object; another is the geometric mean of the semi-major and semi-minor axes:

<sup>2</sup> We warn the reader that the definition of ellipticity is not standard across the literature. This definition is consistent with Bernstein & Jarvis (2002), but not with Kaiser et al. (1995).

$$\frac{2}{2} = \frac{\mathbf{T}^P}{2} \frac{1}{1 - \mathbf{e}^2} = \frac{\mathbf{P}}{\det M}; \quad (4)$$

where  $\mathbf{e}^2 = \mathbf{e}_+^2 + \mathbf{e}_-^2$ . The energy functional is minimized by requiring:

$$M = 2 \frac{\int_{-R}^R (r - r_0)(r - r_0)^T I(x; y) e^{-2x^2} dx dy}{\int_{-R}^R I(x; y) e^{-2x^2} dx dy}; \quad (5)$$

if the centroid were also determined adaptively, we would simultaneously solve

$$Z = \int_{-R}^R (r - r_0) I(x; y) e^{-2x^2} dx dy; \quad (6)$$

However the SDSS photometric pipeline (photo) uses  $r_0$  at the object center's centroid rather than iteratively solving Eq. (6). We also use the radial fourth moment  $a_4$  defined by:

$$2(1 + a_4) = \frac{\int_{-R}^R I(x; y) e^{-2x^2} dx dy}{\int_{-R}^R I(x; y) e^{-2x^2} dx dy}; \quad (7)$$

Photo computes the adaptive moments  $M$  and  $a_4$  for both the observed (i.e. not deconvolved) galaxy image  $I(x; y)$  and the reconstructed PSF  $P(x; y)$ . We will denote moments corresponding to the galaxy image with a superscript  $^{(I)}$  and those corresponding to the PSF with a superscript  $^{(P)}$ . The (raw) resolution factor  $R_2$  is defined by:

$$R_2 = 1 - \frac{T^{(P)}}{T^{(I)}}; \quad (8)$$

in the limit of a very well-resolved galaxy,  $R_2 \approx 1$ , whereas for a poorly resolved galaxy the observed image is very similar to the PSF ( $I \approx P$ ) and so  $R_2 \approx 0$ .

The physical interpretation of  $M^{(I)}$  is as a best-fit Gaussian to the image profile. The fourth moment  $a_4^{(I)}$  parameterizes the departure of the galaxy from Gaussianity: it is 0 for a Gaussian profile, 0.17 for an exponential profile, and 0.40 for a de Vaucouleurs profile. The fourth moment of the PSF diagnoses the deviation of the PSF from Gaussianity. In particular, a PSF dominated by Kolmogorov turbulence (optical transfer function  $\propto e^{-(l-l_0)^{5/3}}$ ; Kaiser 2000) should have  $a_4^{(P)} \approx 0.046$ , in good agreement with the typical PSF in the SDSS.

### 3.1.2 Source galaxy selection

Our source galaxies are selected from the SDSS photometric catalog (York et al. 2000; Hogg et al. 2001; Stoughton et al. 2002; Smith et al. 2002; Pier et al. 2003; Abazajian et al. 2003). The catalog is based on images from the SDSS camera (Gunn et al. 1998) processed at Princeton by the photo software (Lupton et al. 2001; Finkbeiner et al. 2004; Lupton et al. 2004). In order to avoid the PSF anisotropy-induced selection bias discussed by Kaiser (2000) and Bernstein & Jarvis (2002), photo applies a convolution to each image to circularize the effective PSF before running the object detection algorithm. We only consider objects that are classified by photo as galaxies, are not deblended, do not contain saturated pixels, and do not have flags set indicating possible problems with the measurement of the image. We reject objects whose adaptive moment measurements failed, the resolution factor  $R_2 < \frac{1}{3}$ , the measured

ellipticity  $e_+^{(I)2} + e_-^{(I)2} > 0.95$ , or the radial fourth-moments  $\mathbf{p}_4^{(I)} \mathbf{j} > 0.99$  or  $\mathbf{p}_4^{(P)} \mathbf{j} > 0.99$  in at least two of the  $g$ ,  $r$ , and  $i$  bands. Objects with extinction-corrected magnitude fainter than 21 in  $r$ -band or with failed photometric redshifts (see x3.3) are also rejected. In case of multiple observations of the same object, we take the observation where the  $i$ -band resolution factor is largest.

Our final source galaxy catalog contains  $N_s = 6,975,528$  galaxies, although some of these are in regions of the SDSS without spectroscopic coverage and hence are not actually used in the analysis.

### 3.1.3 Measurement of galaxy ellipticities

Since most galaxies used in weak lensing measurements are of comparable angular size to the PSF, the ellipticity ( $e_+^{(I)}; e_-^{(I)}$ ) determined from the galaxy image  $I(x; y)$  is generally not equal to the true ellipticity of the galaxy. Therefore a correction for the PSF is necessary. The basic idea of any such correction is to treat the observed galaxy image  $I$  as a convolution of the PSF  $P$  and a preseeing image  $f$ :

$$I(x; y) = \int_{-R}^R f(x^0; y^0) P(x - x^0; y - y^0) dx^0 dy^0; \quad (9)$$

The problem is to determine the ellipticity of the preseeing image  $f$  from  $I$  and  $P$ . This problem has been considered by many authors (Kaiser et al. 1995; Luppino & Kaiser 1997; Kaiser 2000; Bernstein & Jarvis 2002; Refregier & Bacon 2003; Hirata & Seljak 2003); we use the "linear" method of Hirata & Seljak (2003) because it can be implemented using the photo outputs.

The "linear" method is based on the observation that if the galaxy and PSF are Gaussian, then the adaptive second moment matrix of  $I$  is related to that of the PSF and the preseeing image by:

$$M^{(I)} = M^{(f)} + M^{(P)}; \quad (10)$$

implying:

$$e^{(f)} = \frac{e^{(I)}}{R_2} + (R_2^{-1} - 1)e^{(P)}; \quad (11)$$

Hirata & Seljak (2003) made the approximation that the preseeing galaxy image and the PSF can be approximated by the quartic-Gaussian form:

$$f(x; y) / \sqrt{1 + \frac{a_4}{2} (x^4 - 4x^2 + 2)} e^{-x^2/2}; \quad (12)$$

where  $a_4$  is given by Eq. (7), and similarly for  $P(x; y)$ . Within this approximation, we can compute the corrections to Eq. (10) to first order in  $a_4^{(I)}$  and  $a_4^{(P)}$ . The calculation is straightforward (although tedious) and is given in Appendix B of Hirata & Seljak (2003); it results in a correction to the resolution factor  $R_2$ . We compute ellipticity estimators ( $e_+^{(f)}; e_-^{(f)}$ ) using the formulas presented there. Measurement errors on  $M^{(I)}$  are computed by photo from the Fisher matrix, and propagated into errors on  $e^{(f)}$  via numerical differentiation of the PSF correction formulas.

The actual image of the galaxy and the reconstructed PSF are both pixelized, and in principle the PSF correction should take this into account. Mathematically, pixelization is a two-step process consisting of convolution with a square

top-hat function (i.e. integration over the pixel area), followed by sampling at the center of each pixel. So long as the convolution step is applied to both the PSF and the galaxy, it does not cause concern for us because Eq. (9) is still valid. The sampling at the center of each pixel replaces the integration in the moment computation with summation over pixels, which causes a problem for the integrals in Eq. (5) if the integrand is insufficiently sampled (i.e. if there is a high-wavenumber component aliased to zero wavenumber); this occurs for wavenumbers:

$$1 > l_{\text{alias}} = \frac{2}{\text{pixel}} \quad 3.28 \quad 10 \quad 15.9 \text{ arcsec}^{-1}; \quad (13)$$

A aliasing is more likely to occur for the PSF measurement than the galaxy measurement since the PSF is smaller in real space. If the PSF were a Gaussian with  $\text{FWHM} = 1.2 \text{ arcsec}$  (better than typical seeing in the SDSS), the function  $P(r)e^{-r^2/2}$  (where  $r^2$  is determined from Eq. 2 using  $M^{(P)}$ ) has a width of 0.36 arcsec in real space and 2.8 arcsec<sup>-1</sup> in Fourier-space. Therefore, we do not expect a significant contribution to the moment integrals at the aliasing wavenumber  $l_{\text{alias}}$ , and we have not applied any correction for pixelization.

We have determined the camera shear via differentiation of the SDSS astrometric solution (Pier et al. 2003), and found it to be < 0.2 per cent in all three bands ( $g, r, i$ ) used for the ellipticity measurement in all six camera columns. Given that the camera shear is small and is not correlated with the locations of lens galaxies, no correction for camera shear has been applied. Our search for a shear signal around random points (Sec. 5.2) produced a null result, confirming that camera shear contamination of the intrinsic alignment signal is negligible.

The ellipticities  $e^{(f)}$  are measured separately in the  $g, r$ , and  $i$  bands (the  $u$  and  $z$  bands typically have lower signal-to-noise and so are not as useful for ellipticity measurement). An overall ellipticity is computed for each source galaxy by performing an average (weighted by the measurement error) of the ellipticities in the bands in which ellipticity measurement was successful. At this stage we reject objects with ellipticities  $e^{(f)2} > 2$ .

### 3.1.4 Ellipticity to shear conversion

Once the ellipticities of the source galaxies have been determined, it is necessary to convert them into a shear estimator. The simplest such estimator is obtained by dividing the ellipticity by an appropriate "shear responsivity factor"  $R$ :

$$R = \frac{P_{N_s} \sum_{j=1}^{N_s} \hat{e}_j}{R N_s}; \quad (14)$$

where  $N_s$  is the number of source galaxies measured. Here  $R$  measures the response of the mean ellipticity to an applied shear,  $\hat{e}_j = R + O(\epsilon^2)$ . It is given by: (Bernstein & Jarvis 2002)

$$R = 2(1 - \hat{e}_{\text{rms}}^2); \quad (15)$$

where  $e_{\text{rms}}$  is the RMS ellipticity per component (+ or -). From Fig. 3, we find  $e_{\text{rms}} = 0.37$ . (The factor of 2 comes from the fact that a shear of 1 per cent, when applied to a circular object, yields an ellipticity of 2 per cent.)

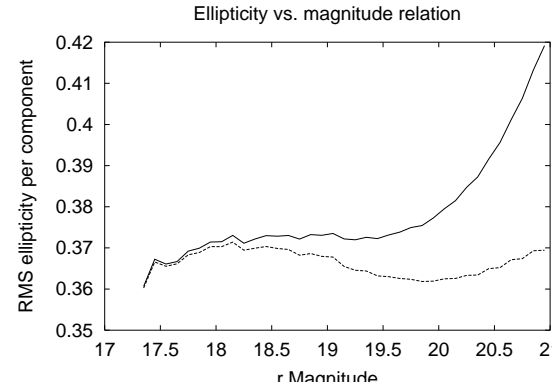


Figure 3. The measured RMS ellipticity of our galaxies per component (i.e. not the total RMS ellipticity, which is  $\sqrt{2}$  times greater since ellipticity has 2 components) as a function of magnitude. The solid curve is the RMS of the measured ellipticities, while for the dashed curve the measurement noise has been subtracted out. For brighter galaxies, the RMS ellipticity per component is 0.37, which is the value we use to compute the shear responsivity. (The statistical significance of the downward dip at  $r = 20$  is large, but its amplitude is only 3 per cent, which makes it smaller than possible calibration errors. It is therefore possible that this does not represent a real feature in the galaxy ellipticity-magnitude distribution.)

In principle, better shear signal-to-noise ratio can be obtained if galaxies are weighted according to the ellipticity measurement error (Fischer & Tyson 1997; McKay et al. 2001) or if an ellipticity-dependent weight is used (Hoekstra et al. 2000; Kaiser 2000; Bernstein & Jarvis 2002). Since we only use bright ( $r < 21$ ) galaxies, for which the measurement error is subdominant to the shape noise, weighting by measurement error is not helpful. Also, while ellipticity-dependent weighting is useful for measurement of gravitational shear, it complicates the interpretation of intrinsic alignment studies since the apparent shear from intrinsic alignments probably depends at some level on the method of weighting. Therefore in this paper we use only the "unweighted" estimator, Eq. (14).

Because there is insufficient signal-to-noise ratio for a shear measurement around one galaxy, we report the shear measurement averaged in annular bins around many lens galaxies. We compute the galaxy-apparent shear correlation function  $\langle t(r) \rangle$  averaged in the annular bin  $r < r < r_+$  by pair summation,

$$\langle t(r; r_+) \rangle = \frac{\sum_{j=1}^{N_p(r; r_+)} t_{j; j}}{N_p(r; r_+)}, \quad (16)$$

where the summation is over lenses and sources  $j$ ;  $N_p(r; r_+)$  is the number of lens-source pairs with separations between  $r$  and  $r_+$ ; and  $t_{j; j}$  is the + component of the apparent shear of source  $j$  in coordinates where the x-axis is aligned perpendicular to the line connecting the lens and source, and the y-axis is aligned along the line connecting the lens and source. That is,  $t$  is the "tangential" shear component (so that lensing-induced shears are positive). In addition to  $t$ , we report the shear  $t_{45}$  at a 45 degree angle to the lens (the - component in the coordinate system aligned with the lens-source direction). The latter must van-

ish in the mean by symmetry, but is nevertheless useful for constraint of the uncertainty estimates.

### 3.2 Calibration uncertainty

In order to interpret the results of either intrinsic or gravitational lensing shear measurements, we must understand two types of systematic errors in the shear measurements: additive biases, which are independent of the shear signal; and multiplicative or calibration biases, which affect the response of the shear estimator to an actual shear. Additive biases (due, e.g. to PSF ellipticity) constitute a source of spurious power in the shear power spectrum and hence are a serious issue for cosmic shear surveys that aim to measure this power spectrum. However, since we are essentially computing a cross-correlation function between the galaxy density and shear, the additive bias can be determined by repeating the galaxy-shear correlation function measurement using a random "lens" galaxy catalog (see Sec. 5.2). Computing the calibration bias is much harder since there is no straightforward way to measure it directly. At present, then, the calibration bias must be understood theoretically by considering all known sources of calibration error. The major sources of error are shown in Table 1 along with their estimated uncertainty. Note that these systematic error estimates are in some cases very rudimentary and should be considered only as rough guides to the level at which systematics might be affecting our results.

In addition to the sources of error mentioned in the table, there are two other phenomena in weak lensing surveys that can mimic a calibration error: source redshift errors and stellar contamination. An error in the source redshift distribution results in incorrect determination of the lensing strength  $c^1$  and hence the surface density contrast  $\delta$ ; however, as our objective here is to measure apparent shear rather than mass, this effect is not relevant to the intrinsic alignment estimation. Stellar contamination of the "source galaxy" sample can dilute the shear signal, resulting in an effective calibration bias in galaxy-galaxy lensing, however this does not affect our measured intrinsic shear signal because we divide our intrinsic shear signal by the fraction of our sources that are physically associated with the lens (as determined by the lens-source correlation function or "pair ratio," see Sec. 5). Stars are not clustered around the lens galaxies and so their dilution effect on the observed shear and the physically associated fraction cancel out in the estimate of  $\delta$ .

In the remainder of this section we discuss each of the biases in Table 1. In each case, our aim is to estimate or constrain the induced calibration bias  $\delta$ , defined by:

$$-\frac{1}{2} \frac{\langle \delta h^+ \rangle_i}{\langle \delta \rangle} + \frac{\langle \delta h^- \rangle_i}{\langle \delta \rangle} = 1; \quad (17)$$

where  $h^\pm_i$  is the expectation value of the shear estimator. Note that  $\delta = 0$  for an unbiased shear estimator ( $\langle h^\pm \rangle_i = 0$ ). If  $\delta$  is positive, then any galaxy-shear correlation signal will be overestimated; if  $\delta$  is negative, the signal will be underestimated. In principle,  $\delta$  may vary with angular position, however in computing the effective calibration bias for the galaxy-shear correlation we only care about the average value of  $\delta$ .

Table 1. Identified sources of calibration error  $\delta$  in the apparent shear measurement, and rough upper limits to the level of error they might induce. (See text for caveats.)

Source	Calibration error (per cent)
PSF dilution correction	8 to +6
PSF reconstruction	1.9
Shear selection bias	5.0
Shear responsivity error	1.7
Noise-rejection bias	1.1 to +1.4
Total	18 to +16

#### 3.2.1 PSF dilution correction

As noted in Sec. 3.1.3, we do not measure the galaxy ellipticity  $e^{(f)}$  directly but rather the measured image ellipticity  $e^{(I)}$ , which has been diluted by the blurring effect of the PSF. Our correction for this effect is not perfect since the quartic-Gaussian form (Eq. 12) is not a perfect model for the ellipticity of the galaxy or PSF, and this can lead to a calibration error.

The calibration error in the PSF dilution correction for adaptive moment methods was studied in detail in Hirata & Seljak (2003) (an analysis for the non-adaptive moment methods can be found in Erben et al. 2001). Hirata & Seljak (2003) found that for the range of parameters of interest here, the "linear" correction can have calibration bias between -8 and +13 per cent (the worst case being exponential-profile galaxies whose resolution factor is near our limit  $R_2 > \frac{1}{3}$ ). However, we note that for 81 per cent of our source galaxies,  $R_2 > \frac{1}{2}$ , and within this range Hirata & Seljak (2003) found that  $\delta$  ranges from -8 to +4 per cent. Using this tighter constraint for the  $R_2 > \frac{1}{2}$  galaxies, and the -8 to +13 per cent range for the 19 per cent of our sample with  $\frac{1}{3} \leq R_2 \leq \frac{1}{2}$ , we constrain  $\delta$  for the overall sample to lie in the range of -8 to +6 per cent. This is the range of values shown in Table 1.

It can be seen from Table 1 that the PSF dilution correction is currently the largest item in the calibration error budget; this error will be reduced in future studies by using more accurate but computationally expensive PSF correction methods such as re-Gaussianization (Hirata & Seljak 2003) or shapelet decomposition (Refregier 2003; Refregier & Bacon 2003).

#### 3.2.2 PSF reconstruction

The SDSS PSF is reconstructed using images of the bright stars by the psp pipeline (Stoughton et al. 2002). Any error in the PSF model used in the PSF correction can translate into an error in the "PSF-corrected" ellipticity  $e^{(f)}$ . Two major types of error concern us here: ellipticity errors and trace (size) errors. Ellipticity errors introduce spurious power into the shear measurements, which can be a serious problem for shear autocorrelation measurements (Jarvis et al. 2003; Hoekstra 2004); however to lowest order these are less serious for galaxy-galaxy lensing because these errors are not expected to correlate with the locations of galaxies. If the size  $T^{(P)}$  of the PSF is systematically over- or underesti-

imated, this leads respectively to under- or overestimation of the ellipticity  $e_{\pm}^{(f)}$ , and hence to a shear calibration error. We have tested the PSF traces by comparing them to the observed traces  $T^{(I)}$  of "stars" (as identified by photo) with PSF magnitude uncertainty<sup>3</sup> in the range 0.05–0.1 (1.). Fainter stars are not used because their moments are too noisy; brighter stars are not used because they have been used as part of the PSF fitting and hence the errors in their moments may not be representative of the typical error in PSF reconstruction.

An estimate of the systematic error in the PSF trace can be obtained by considering the quantity  $q = \ln(T^{(I)} - T^{(P)})$ . If the PSF reconstruction were perfect, we would have (to second order in  $T^{(I)} = T^{(I)} - T^{(P)}$ ):

$$hq_i = \frac{h T^{(I)} i}{T^{(P)}} - \frac{1}{2} \frac{h T^{(I)2} i}{T^{(P)2}} = \frac{2}{2}; \quad (18)$$

where  $h$  is the signal-to-noise ratio, and we have used Eq. (C26) for the bias and variance of the adaptive trace estimator, assuming the ellipticity of the PSF is small compared to unity. The signal-to-noise ratio, for near-Gaussian PSF, is related to the PSF magnitude uncertainty  $_{\text{PSF mag}}$  via  $h = 0.4 \ln 10 = _{\text{PSF mag}}$ . Thus the log trace ratio  $q$  has expectation value

$$hq_i = 0.0236 \frac{_{\text{PSF mag}}^2}{0.1} + O(\frac{3}{_{\text{PSF mag}}}); \quad (19)$$

which varies from 0.0059 to 0.0236 over the range of signal-to-noise ratios considered.

The tail-rejected means obtained from the stars are  $hq_i = 0.0087$ ,  $0.0086$ , and  $0.0086$ , in  $g$ ,  $r$ , and  $i$  respectively if objects more than 3 from the mean are rejected; and  $+0.0057$ ,  $+0.0057$ , and  $+0.0056$  (with rejection at 7). Comparison of these numbers to Eq. (19) suggest that the systematic bias in  $q = \ln(T^{(I)} - T^{(P)})$  induced by PSF reconstruction errors is 6.3 per cent, i.e. that if  $T^{(P)}$  is being systematically over- or under-estimated by psp then the magnitude of this effect is no more than 3 per cent. We have therefore computed the systematic error in Table 1 assuming  $T^{(P)} = T^{(P)} = 0.03$ . The conversion to a shear calibration is obtained by differentiation of Eq. (11) with respect to  $T^{(P)}$ , neglecting the non-Gaussian correction to  $R_2$ . This yields, to first order,

$$\frac{e_{\pm}^{(f)}}{e_{\pm}^{(f)}} = \frac{R_2}{R_2} = (R_2^{-1} - 1) \frac{T^{(P)}}{T^{(P)}}; \quad (20)$$

(The error for  $e$  is the same.) The mean value of  $R_2^{-1} - 1$  for our sample of galaxies is 0.62; multiplying by 0.03 gives the systematic error estimate in Table 1.

### 3.2.3 Shear selection bias

If the algorithm for selecting galaxies preferentially selects galaxies that are nearly circular, then the estimated shear (as computed from Eq. 14) will be closer to zero than the true shear. This could arise, e.g. because after PSF convolution a circular galaxy is spread over fewer pixels (and hence

<sup>3</sup> The PSF magnitude of an object is computed by fitting a PSF to the image of the object and finding the best-fit normalization.

will be detected at higher signal-to-noise) than a highly elongated galaxy with the same magnitude and pre-selecting area.

The shear selection bias is difficult to compute from first principles because of cuts made on the galaxy sample (convergence of adaptive moments, ages, resolution factor cut, ellipticity cut, etc.). Of these, the most worrying are the resolution factor cut and the adaptive moment convergence. In general, the shear selection bias is given by (Hirata & Seljak 2003):

$$\frac{+}{+} = \frac{1}{R} e_{\pm}^{(f)} \frac{\theta}{\theta} \ln P; \quad (21)$$

where the average is taken over galaxies used for the measurement;  $P$  is the probability of a galaxy being detected and selected;  $e$  is the ellipticity of the galaxy; and  $\theta$  is the gravitational shear. (A similar equation holds for  $-$ .) Conceptually, this equation is telling us that if the selection probability is decreased by applying an infinitesimal shear that makes the galaxy more elliptical, then the shear will be underestimated.

Given the absence of a good theoretical model of selection biases, we parameterize the problem by assuming that there is a selection probability that is a function of the ellipticity,  $P(e)$ , and that we may approximate  $\ln P(e)$  using a polynomial of order 2 :

$$\ln P(e) = \sum_{j=0}^X c_{2j} e^{2j}; \quad (22)$$

(Odd-order terms in  $e$  are forbidden by symmetry.) The distribution of galaxy ellipticities is shown in Fig. 4(a). In Fig. 4(b), we have added noise to the ellipticities so that all the galaxies have the same ellipticity noise  $e = 0.25$  (i.e. we have added random increments  $e_{\pm}$  and  $e$  of variance  $0.25^2$  to each component of the ellipticity). If we assume that the difference between the  $r < 19.0$  and  $20.5 < r < 21.0$  curves in Fig. 4(b) is entirely due to selection biases, then we should have:

$$\ln \frac{n_{20.5 < r < 21.0}(e)}{n_{r < 19.0}(e)} = \sum_{j=0}^X c_{2j} e^{2j} + \text{const}; \quad (23)$$

Fit to this equation in the range  $0 < e < 1.5$  using  $X = 4$  (parameters) gives  $c_2 = 0.0178$ ,  $c_4 = 0.281$ ,  $c_6 = +1.140$ , and  $c_8 = +0.205$ . (We fit beyond the maximum  $e = 1.414$  used in this paper to suppress the characteristic "ringing" of polynomials.) Substituting this fit into Eq. (21), and noting that  $de = 2e_{\pm}(1 - e^2)$ , we find that the shear selection bias is:

$$\frac{+}{+} = \frac{1}{R} e(1 - e^2) n(e) \frac{d \ln P}{de} de \stackrel{!}{=} \frac{1}{R} \int_0^{e_{\text{max}}} (1 - e^2) n(e) \sum_{j=1}^X 2j c_{2j} e^{2j} de; \quad (24)$$

For the  $20.5 < r < 21.0$  magnitude range, we compute  $= +0.025$ . We find that the computed  $=$  remains between 0.02 and 0.03 as we adjust the order of the fitting polynomial from 4 ( $X = 2$ ) to 20 ( $X = 10$ ), indicating that the polynomial is not affecting the results. The error given in Table 1 is 5.0 per cent, which is twice the error obtained from Eq. (24) (to give a more conservative estimate). We

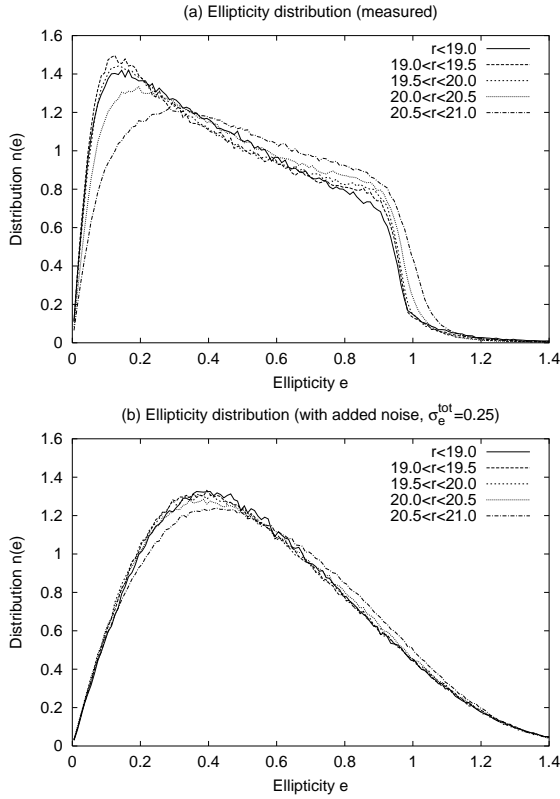


Figure 4. (a) The distribution of measured PSF-corrected ellipticity  $e^{(f)} = \sqrt{e_x^2 + e_y^2}$  of source galaxies as a function of  $r$  and magnitude. Each curve has been separately normalized to  $n(e)de = 1$ . (b) The same distribution, except that each galaxy has had noise added to both ellipticity components so that the total noise is  $\sigma_e = 0.25$  per component. This allows us to directly compare the various ellipticity distributions, since differences among them are not due to variations in  $\sigma_e$ . A small number (ranging from 0.3 per cent at  $r < 19$  to 7 per cent at  $20.5 < r < 21.0$ ) of objects had  $e > 0.25$ ; no noise was added to their ellipticities.

emphasize that we are placing a constraint on the selection bias, and that we have not found evidence that this bias is in fact present. In particular, the differences between the curves in Fig. 4(b) could also be due to the small number of objects with large  $e$  (so that their ellipticity noises could not be 'boosted' to 0.25); non-Gaussianity of the ellipticity error distribution; systematic errors in ellipticity measurement (perhaps due to PSF effects); a real variation in the source ellipticity distribution with apparent magnitude; or some combination of these effects.

#### 3.2.4 Shear responsivity error

Any error in  $\epsilon_{\text{rm}\,s}$  translates into an error in the shear responsivity  $R$  via Eq. (15) and hence an error in the calibration of Eq. (14). While the statistical uncertainty in  $\epsilon_{\text{rm}\,s}$  is negligible because we have millions of source galaxies, the systematic uncertainty must be taken into account. An error  $\epsilon_{\text{rm}\,s}$  thus translates into a calibration error given by:

$$\frac{\Delta R}{R} = \frac{2\epsilon_{\text{rm}\,s}\epsilon_{\text{rm}\,s}}{1-\epsilon_{\text{rm}\,s}^2} = 0.86\epsilon_{\text{rm}\,s}: \quad (25)$$

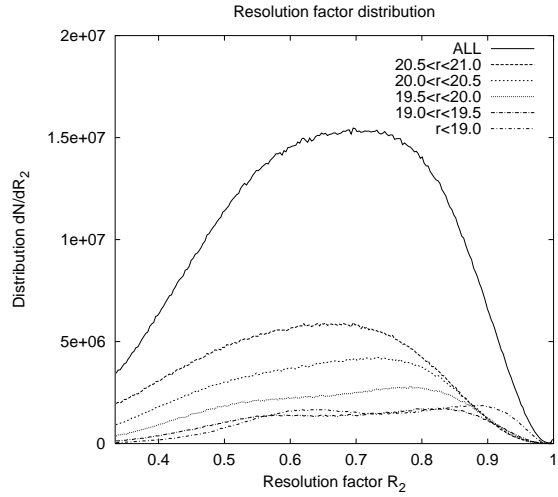


Figure 5. The distribution of source galaxy resolution factors,  $dN = dR_2 = N_{\text{sn}}(R_2)$ .

From Fig. 3, we take  $\epsilon_{\text{rm}\,s} = 0.02$  as a reasonable error estimate; if the error in  $\epsilon_{\text{rm}\,s}$  is larger than this then it must either cancel a magnitude dependence of the rms ellipticity or else it must affect objects of all magnitudes similarly (which is unlikely because the resolution factor  $R_2$  is strongly correlated with magnitude). This leads to the error estimate from shear responsivity error of  $\Delta R/R = 0.017$ , as given in Table 1.

#### 3.2.5 Noise-rectification bias

The fitting to determine  $M^{(I)}$ , and the subsequent PSF correction to obtain  $e^{(f)}$ , are nonlinear operations, hence noise in the original image  $I(r)$  can lead to a bias in the ellipticity  $e^{(f)}$ . The additive bias (spurious power) introduced by noise rectification has been previously noted in the context of cosmological shear surveys (Kaiser 2000; Bernstein & Jarvis 2002). Here we consider the effect of noise rectification on calibration bias. This effect has not been previously analyzed, although it is present implicitly in simulations (e.g. Bacon et al. 2001; Erben et al. 2001).

The calibration correction due to noise-rectification bias is proportional to the noise variance and hence to  $\sigma_e^2$ , where  $\sigma_e$  is the detection significance of the galaxy, i.e.:

$$- K_N \sigma_e^2 + O(\sigma_e^3): \quad (26)$$

The noise-rectification coefficient  $K_N$  is evaluated in Appendix C, and found to be (compare to Eq. C27):

$$K_N = 4(1 - 3R_2^{-1} + R_2^{-2} + 2\epsilon_{\text{rm}\,s}^2): \quad (27)$$

Our galaxies have resolution factor  $\frac{1}{3} < R_2 < 1$  and  $\epsilon_{\text{rm}\,s} = 0.37$ . Within this range,  $K_N$  takes on a minimum value of 3.9 at  $R_2 = \frac{2}{3}$  and a maximum value of +5.1 at  $R_2 = \frac{1}{3}$ . A typical  $r = 21$  galaxy in moderate (1.7 arcsec FWHM) seeing has  $R_2 = 10, 25$ , and  $20$  in the  $g, r$ , and  $i$  bands, respectively. The bands are weighted by ellipticity error  $\sigma_e^2$ , which is proportional to  $\sigma_e^2$  assuming the resolution factors in the three bands are all equal. In this case, the weighted mean  $\sigma_e^2$  is:

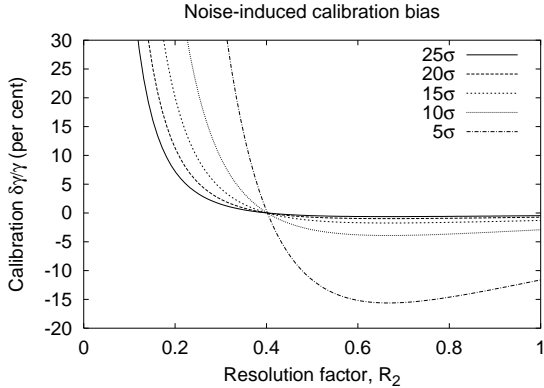


Figure 6. The calibration bias obtained from Eq. (C27) for  $e_{\text{rm}} s = 0.37$ , as a function of resolution factor  $R_2$  and detection signal-to-noise ratio  $= 5::25$ . Note the large bias for poor resolution factors  $R_2 < 1/3$  and low signal-to-noise. The zero crossing at  $R_2 = 0.4$  is somewhat dependent on  $e_{\text{rm}} s$  and only exists for the first term in the asymptotic expansion of Eq. (26), hence this plot should not be taken as an indication that weak lensing measurements are best done with galaxies of this resolution factor.

$$h^2 i_{\text{weighted}} = \frac{3}{g^2 + r^2 + i^2}; \quad (28)$$

which for the signal-to-noise ratios listed above case is 0.0027. The product  $K_N^{-2}$  appearing in Eq. 26 is thus between 0.011 and +0.014. This is shown as the upper limit in Table 1.

While the noise-induced calibration bias (Eq. 26) is a subdominant source of error in this investigation, the same may not be true of all lensing observations. For example, for sources detected at 10 ( $= 10$ ) and resolution factor  $R_2 = 0.2$ , we find  $= +0.44$ , which likely dominates the calibration error budget for these sources (see Fig. 6). The lensing studies that use these low-significance objects usually down-weight them due to their large ellipticity uncertainty  $e$ , so the noise-induced calibration bias in the final result could still be small. However in this situation the ellipticity estimator  $\hat{e}^{(f)}$  can be correlated with the weight, which leads to additional terms (positive or negative) in the calibration. The analysis of these correlations and their induced calibration bias is not needed here and is deferred to future work.

### 3.3 Source photometric redshift samples

It is critical for weak lensing experiments to have accurate knowledge of the source redshifts (and the lens redshifts, in the case of galaxy-galaxy lensing studies). It is also useful for studies of the intrinsic correlations, since it enables us to distinguish physically associated pairs from widely separated pairs for which the gravitational lensing effect dominates the galaxy-apparent shear correlation. In this investigation, we have used spectroscopic redshifts for the lens galaxies and photometric redshifts for the source galaxies. This section describes the methodology used to determine the photometric redshifts, and briefly considers some of tests of the photometric redshifts. Photometric redshift tests will be discussed in more detail in Mandelbaum et al. (2004).

#### 3.3.1 Methodology

Photometric redshift algorithms using the five SDSS bandpasses ( $u, g, r, i$ , and  $z$  centered at 354, 475, 622, 763, and 905 nm, respectively; Fukugita et al. 1996) have previously been developed (Cirasuolo et al. 2003). These photometric redshifts are based on the "hybrid" photometric redshift methods (Cirasuolo et al. 2000; Budavari et al. 2000), in which the spectral energy distribution (SED) templates are parameterized; the SED parameters and source redshifts are then simultaneously fit to the photometric data. These are only available for some regions of sky (specifically the 2099 deg<sup>2</sup> covered by the SDSS Data Release 1, hereafter DR1). Fortunately, this error does not significantly affect the model colors, and the photometric redshifts are derived by fitting the colors of each source galaxy to the template SEDs. We have therefore used the following methodology to derive photometric redshifts: the DR1 galaxies in our sample are placed in the 5-dimensional ugriz-space. For each source galaxy outside of the DR1 coverage, we identify the nearest neighbour in ugriz-space with a computed photometric redshift:

$$s = \sqrt{u^2 + g^2 + r^2 + i^2 + z^2}; \quad (29)$$

We report a photometric redshift failure if the nearest neighbour lies at distance  $s > 0.1$  in ugriz-space. Of the 8,574,845 galaxies with measured ellipticities and  $r < 21$  that pass the mag cuts, matches are found for 6,925,528 (including DR1 objects). The separation  $s < 0.05$  for 5,889,951 of these galaxies, including the 3,046,566 galaxies used to construct the nearest-neighbour points.

#### 3.3.2 Pair ratio tests

The pair ratio  $R_p(r)$  (Eq. A2) is a useful tool for testing photometric redshifts; it is defined for a given transverse separation and lens luminosity as the ratio of the number density of "source" galaxies in a given redshift slice at that transverse separation to the number density found in the field. We split the lens-source pairs into widely separated ( $z_s > z_l + \Delta z$ , where  $\Delta z = 0.05$  or  $0.1$ ) and nearby ( $|z_s - z_l| < \Delta z$ ) samples. If the photometric redshifts were perfect, we would have  $R_p(r) = 1$  for the  $z_s > z_l + \Delta z$  samples (the exception to this is the magnification bias effect, which should be of the same order of magnitude as the shear, i.e. of order 1 per cent). For the  $|z_s - z_l| < \Delta z$  samples, we expect  $R_p(r) > 1$  due to galaxy clustering.

We compute the pair ratio by dividing the number of lens-source pairs per unit area by the value obtained from randomly generated (Poisson) lens catalogs:

$$R_p(r) = \frac{n(r)}{n_{\text{rand}}(r)}; \quad (30)$$

where  $n(r)$  is the number of lens-source pairs per unit area in a given radial bin. The large  $R_p$  for the  $|z_s - z_l| < \Delta z$  samples is easily seen in Fig. 7, and it is greatly suppressed in the  $z_s > z_l + \Delta z$  samples. The density of source galaxies varies considerably with seeing because of our resolution factor and signal-to-noise cuts. If the lens selection algorithm were perfectly independent of seeing, this would not contaminate the pair ratio (which is essentially a cross-correlation between lenses and sources), but slight variations in the lens number density with seeing could cause

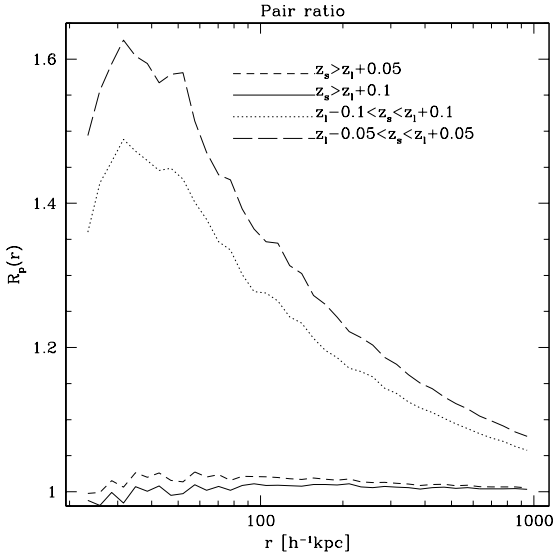


Figure 7. Pair ratio for several samples, as indicated on the plot.

a systematic effect (positive or negative) on  $R_p(r)$ . However, in the widely separated samples the combined effect of any seeing systematics and lens-source clustering (due to photometric redshift errors) is  $R_p(r) \approx 1$  in the innermost bins ( $r < 100h^{-1}$  kpc) and  $< 1$  in the outer bins ( $r > 1000h^{-1}$  kpc). When we split the lenses into different magnitude ranges, we find  $R_p(r) \approx 1$  in all magnitude ranges except for  $M_r < -22$ , where  $R_p$  ranges from 1.2 (in  $30 < r < 100h^{-1}$  kpc) to 1.04 (in  $300 < r < 992h^{-1}$  kpc). This excess is more likely to be a result of photometric redshift errors than systematics in the source density because it is much more significant at small radii and for the brighter lenses. This suggests that the seeing systematics in  $R_p(r)$  is at the 1–3 per cent level or less.

As another test of the photometric redshifts, Fig. 8 shows a plot of the pair ratio for galaxies at  $0 < z_s < z_l$ . This sample should also include no physically-associated pairs, and therefore should have  $R_p$  near 1. Instead, there is a large pair ratio at small radii, indicating that some physically-associated galaxies at higher redshift are erroneously assigned to very low redshift. (We examined the pair ratio in the range  $0.003 < z_s < z_l$  to eliminate objects assigned to very low photometric redshift; this did not reduce the pair ratio, and so we have not imposed this cut in any of the results presented in this paper.) Fortunately, however, the actual number of source galaxies represented by the excess pair ratio in Fig. 8 is relatively small. To see this, we compute the excess number of galaxies in the  $0 < z_s < z_l$ ,  $z_l < z < z_l + \Delta z$ , and  $z_s > z_l + \Delta z$  samples:

$$\begin{aligned} N_+ &= (N - N_{\text{rand}}) [z_s > z_l + \Delta z] \\ N_0 &= (N - N_{\text{rand}}) [z_l - \Delta z < z < z_l + \Delta z] \\ N_- &= (N - N_{\text{rand}}) [z_s < z_l - \Delta z]; \end{aligned} \quad (31)$$

and compute the normalized fractions:

$$f_+ = \frac{N_+}{N_+ + N_0 + N_-}; \quad (32)$$

The fractions  $f_+$ ,  $f_0$ , and  $f_-$  respectively represent the fraction of physically associated source galaxies whose photo-

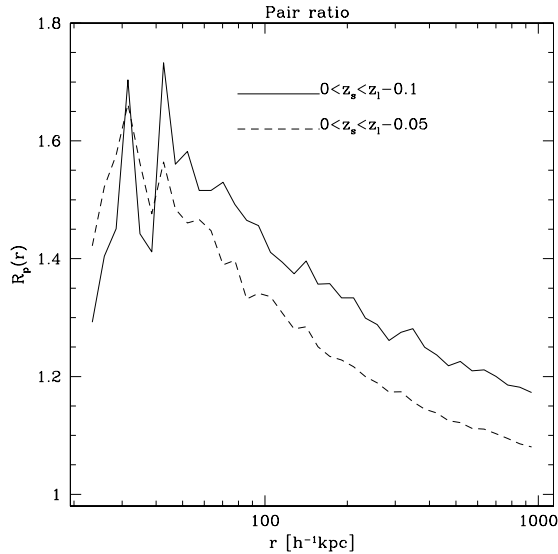


Figure 8. Pair ratio for  $0 < z_s < z_l$ . Counterintuitively, the  $\Delta z = 0.1$  curve is above the  $\Delta z = 0.05$  curve; this is because higher-redshift (and hence more luminous due to the apparent magnitude cut for SDSS spectroscopy) lenses are weighted more heavily when we examine only pairs with the 'source' at lower redshift.

metric redshifts are overestimated, correctly estimated (to within  $\pm 0.1$ ), and underestimated. For the sample of all galaxies at radii  $30 < r < 446h^{-1}$  kpc, we find  $f_+ = 0.13$ ,  $f_0 = 0.82$ , and  $f_- = 0.05$  (for  $\Delta z = 0.1$ ), i.e. only 5 per cent of the source galaxies that are clustered with the lens have redshifts underestimated by more than 0.1. The overestimation and underestimation failure rates increase to  $f_+ = 0.26$  and  $f_- = 0.16$  if we narrow our redshift slice to  $\Delta z = 0.05$ . We find that  $f_\pm$  is an increasing function of lens luminosity, which is expected since (i) the photometric redshift can be an underestimate of the true redshift only if the true redshift exceeds  $\Delta z$ , and (ii) the more luminous lenses tend to be more distant. Another trend that we find is that the 'probability of correct source photometric redshifts'  $f_0$  decreases with increasing transverse separation  $r$  (e.g. for the all lenses,  $\Delta z = 0.1$  sample we have  $f_0 = 0.90$  at  $30 < r < 100h^{-1}$  kpc, decreasing to  $f_0 = 0.80$  at  $300 < r < 446h^{-1}$  kpc), which could be indicative of a variation of satellite galaxy colors as a function of radius. The result that  $f_+ > f_-$  indicates a bias or skewness in the photometric redshift error distribution.

It thus appears that for the sources used in this paper, roughly 40 per cent of the source galaxies physically associated with a lens are scattered outside of  $z_l \pm 0.05$  by photometric redshift errors, and 20 per cent are scattered outside of  $z_l \pm 0.1$ .

### 3.4 Excluded lens-source pairs

At sufficiently small lens-source separation angles, the measurement of sources becomes complicated because the source can overlap with the lens (or with the tail of the PSF convolved with the lens). Problems that occur in this regime can include incorrect ellipticity measurement if overlapping objects are used in the analysis, and selection bias if they are

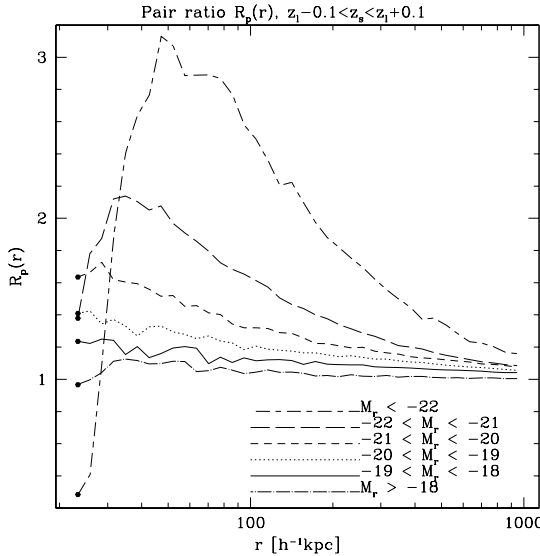


Figure 9. Pair ratio for  $z_s - z_l < 0.1$ , several luminosity sub-samples.

not. In our case deblended objects are not used for ellipticity measurement.

A crude way to determine which annular bins are affected by the overlapping source-lens effect is to examine the pair ratio for source samples selected to be within redshift  $z_s - z_l < 0.1$  of the lens (Fig. 9 for  $z_l = 0.1$ ). The effect of clustering is easily seen: the pair ratio is greater than unity and (over most of the range of radii) increases as the lens magnitude  $M_r$  increases and the transverse separation  $r$  decreases. However, at the innermost radii there is a drop off in  $R_p(r)$  since sources inside these radii are deblended. Brighter galaxies have a more pronounced dip in the excess at the very innermost radii (out to 40 physical  $h^{-1}$  kpc for the very brightest bin), for two reasons: (i) these bright galaxies are typically quite large; and (ii) they are more distant so the same angular separation (relevant to deblending) corresponds to greater physical transverse separation. Padmanabhan et al. (2004) find that for  $M_r = -22$  elliptical galaxies (the fainter edge of this brightest luminosity bin), the typical 50 per cent light radius is  $10h^{-1}$  kpc, in which case there may be significant overlap at the innermost bin ( $r = 20h^{-1}$  kpc). Since the angular diameter distance is  $15z_l h^{-1}$  kpc per arc second, and the typical seeing in the SDSS is 1.2 arc seconds, the deblending effect can increase them in minimum usable radius by tens of  $h^{-1}$  kpc for our brightest sub-sample (typical  $z_l = 0.25$ ). For the faintest sub-sample (typical  $z_l = 0.03$ ), this increase is much less important.

Therefore, for the brightest two luminosity samples ( $M_r < -21$ ), we have rejected the inner bins where  $R_p$  is increasing with  $r$ . (We have verified that rejecting one extra bin or one fewer bin does not significantly affect the final results.)

#### 4 SHEAR UNCERTAINTY ESTIMATION

We use two methods to compute the statistical uncertainty in the shear  $\tau$ . The first is a random lens method, in which

we use our source catalog to compute the covariance of the shear signal around random points within the lens sample region. The second is a bootstrap method in which we cut the lens sample region into 150 subregions that are then resampled. Because both methods use the actual source catalog, they will correctly take into account error from any spurious shear power in the source catalog. The random lens method has the disadvantage of not taking into account fluctuations in the lens number density (particularly if they correlate with the noise or systematics in the source catalog). The bootstrap method addresses these shortcomings on the smallest scales, but suffers due to the fact that the shear signals computed in the 150 subregions are not truly independent, because a source galaxy near a subregion boundary may contribute to the measurement of shear around lenses in multiple subregions. In addition, the noise in the bootstrap covariance matrix (which can have a significant impact on, e.g.,  $\chi^2$  testing) is more difficult to assess. The bootstrap covariance matrix can be made essentially noiseless by taking thousands of subregions, but then the correlations among the subregions become large and the validity of the bootstrap method is undermined.

Given with the deficiencies of either the random lens method or the bootstrap method individually, we have chosen to combine them as follows. The errors on the intrinsic alignment determination are computed using both the random-lens and bootstrap covariance matrices; consistency between the two methods suggests that both are reasonable estimates of the uncertainty. The  $\chi^2$  analysis is performed using the covariance matrix from the random lens catalogs; the effect of noise in the covariance matrix is taken into account as described in Appendix D. The outermost bins in the faintest luminosity sub-samples are excluded from the analysis since galaxy clustering renders the random-lens method inaccurate here, and it is for these bins that the independence of subregions assumed by bootstrap has the least robust justification.

#### 4.1 Random lens method

We compute our statistical errors using a random lens test, which involves computing the shear around random "located lenses," where Poissonian (independent) random lens locations were generated using the angular mask of the survey. We constructed 78 random lens catalogs; the galaxies in each random catalog were assigned magnitudes and redshifts drawn from the true sample without replacement. The covariance matrix between radial bins  $i$  and  $j$  is computed as:

$$\hat{C}_{ij} = \frac{1}{M} \sum_{m=1}^M \frac{1}{1} \langle \tau_i(r_i) \tau_j(r_j) \rangle - \langle \tau_i(r_i) \rangle \langle \tau_j(r_j) \rangle; \quad (33)$$

where  $M = 78$  is the number of random catalogs, the index  $m$  denotes the random catalogs, and  $\langle \tau(r_i) \rangle$  is the sample mean of the shear in radial bin  $i$  averaged over all of the random catalogs. So long as the error distribution of the  $\tau(r_i)$  is jointly Gaussian,  $\hat{C}$  gives an unbiased estimate of the covariance (but it cannot be used naively in  $\chi^2$  tests; see Appendix D). The number of random catalogs used must be  $> N$  (the number of radial bins) in order to produce a non-

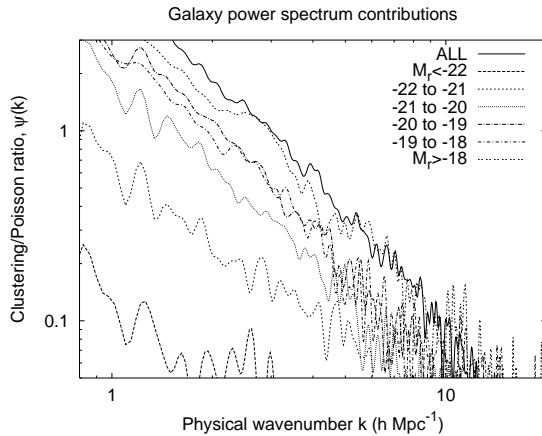


Figure 10. The ratio  $\psi(k)$  of clustering to Poisson contributions to the galaxy power spectrum. This is obtained from the data using Eq. (34), imposing a smooth cutoff in the integrand in the range  $20 \{ 30 \text{ } h^{-1} \text{ Mpc}$ .

degenerate estimator  $\hat{C}$  for the covariance, but is limited by available processor time.

The Poisson-distributed random lens method produces valid error bars on angular scales where the angular (two-dimensional) galaxy power spectrum is Poisson-dominated and the clustering contribution can be safely neglected. Neglecting edge effects in the survey, this range of angular scales can be determined from the ratio of the galaxy clustering power spectrum to the Poisson spectrum:

$$(k) = \frac{P(k; \text{clustering})}{P(k; \text{Poisson})} = \frac{2}{N_{\text{gal}}} \int_0^1 \frac{dN_{\text{p,excess}}}{dr} J_0(kr) dr, \quad (34)$$

where  $N_{\text{gal}}$  is the number of galaxies in the sample,  $k$  is the physical (not comoving) wavenumber of interest,  $r$  is the transverse separation, and  $N_{\text{p,excess}}$  is the number of pairs of galaxies with transverse separation  $r$  minus the number of pairs derived from a random (Poisson) catalog. We use the average of the angular diameter distances to the two galaxies for the conversion of angular separation into transverse separation  $r$  (this should be valid because no correlations should exist between galaxies at very different angular diameter distances). The ratio  $(k)$  is plotted for our samples in Fig. 10.

If we were cross-correlating all of the lens galaxies against the same sample of "source" galaxies, the error variance of the cross-spectrum would simply be re-scaled in proportion to the galaxy power spectrum, i.e. as  $\propto 1/(1+(k))$ . (If survey boundary effects can be neglected it does not matter that we are computing the correlation function via pair summation as opposed to via a cross-spectrum in Fourier space.) If  $(k) \ll 1$ , then the Poisson power spectrum is a good approximation to the lens galaxy power spectrum and hence to the error of  $\tau$ . If  $(k) \gg 1$ , then the lens galaxy power spectrum is much greater than the Poisson estimate, and the error on  $\tau$  for Poisson-distributed lenses is less than the error for "real" clustered galaxies. Thus we expect the Poisson random lens method to be a good way to estimate error bars in the case where  $(k) \ll 1$ . In this paper we are cross-correlating each lens galaxy with the shear of source

Table 2. The number of lens galaxies in each luminosity subsample, and the maximum radius  $r_{\text{max}}$  at which the Poisson random catalog uncertainties are valid. We estimate  $r_{\text{max}}$  from  $r_{\text{max}} = 3.055 = k_{\text{min}}$ , where  $k_{\text{min}}$  is the minimum wavenumber (largest scale) at which  $(k) \approx 0.2$ , i.e. at which the clustering power spectrum is 20 per cent of the Poisson power spectrum.

Subsample	$N_{\text{gal}}$	$r_{\text{max}} (h^{-1} \text{ Mpc})$
all	200747	0.43
$M_r < 22$	11337	$> 1.00$
$22 \leq M_r < 21$	54768	$> 1.00$
$21 \leq M_r < 20$	72464	0.74
$20 \leq M_r < 19$	41276	0.55
$19 \leq M_r < 18$	14475	0.52
$M_r \geq 18$	6427	0.43

galaxies within the redshift slice  $z_1 \leq z \leq z_2$ ; this increases the importance of the clustering contribution. However, for each of our luminosity subsamples, the width of the lens redshift distribution  $z$  is of order 2 (or less, for the lowest-luminosity subsamples), hence  $(k) \approx 1$  is still a valid condition for the clustering to be unimportant. Since the galaxy power spectrum scales roughly as  $P(k; \text{clustering}) \propto k^{-1.2}$ , whereas the Poisson contribution is independent of  $k$ , the clustering contribution dominates on large scales whereas the Poisson contribution dominates on small scales. The random lens method is thus valid only at the smaller scales.

The above reasoning applies in Fourier space. The real-space galaxy-apparent shear correlation function  $\tau(r)$  is related to the galaxy-apparent shear cross-power spectrum by:

$$\tau(r) = \frac{1}{2} \int_0^r k^2 P_g(k) J_2(kr) d \ln k. \quad (35)$$

The  $J_2$  function peaks at  $kr = 3.055$ ; therefore, we take only the annuli out to a distance  $r_{\text{max}} = 3.055 = k_{\text{min}}$  where  $(k_{\text{min}}) = 0.2$ . The values of  $r_{\text{max}}$  are shown in Table 2.

While the clustering of lens galaxies has the effect of increasing our error bars, the clustering of source galaxies around lens galaxies tends to decrease errors because there are more "sources" near the lenses in the real catalog than in the Poisson catalogs. This effect is significant when  $R_p \ll 1$  is of order unity (or larger), i.e. in the innermost  $200 h^{-1} \text{ kpc}$  of our brighter subsamples. It is only important for the source samples whose redshifts are similar to the lens redshifts (the  $z_1 - 0.1 \leq z \leq z_1 + 0.1$  samples) since there is negligible lens-source correlation between different redshifts. We have not applied any source clustering correction in the computation of our error bars, thus our error estimates should be viewed as conservative.

#### 4.2 Bootstrap method

The bootstrap method, as applied here, consists of the following major steps:

- (i) Split the lens catalog into  $M = 150$  subcatalogs containing similar numbers of lens galaxies.
- (ii) Generate  $K = 10^5$  synthesized lens catalogs. Each synthesized lens catalog is a concatenation of  $M = 150$  of the subcatalogs, selected randomly with replacement. (Some

lens galaxies appear in the synthesized catalog multiple times, others not at all.)

(iii) Compute the shear signals  $\mathbf{f}_t^T \mathbf{g}_i^K$  from each of the synthesized catalogs, and compute their covariance  $\hat{\mathbf{C}}_{\text{boot}}$ .

In order to produce subcatalogs that are as independent as possible, we divide galaxies into subcatalogs that consist of different regions of sky. The subcatalog boundaries are based on the SDSS coordinate system (Stoughton et al. 2002). The lens galaxies are first split into 45 rings of width  $\Delta\theta = 4$  degrees bounded by parallels of constant  $\Delta\theta$ . Within each ring, they are then rank-ordered by  $\theta$  (in the range of 180 to  $+180$  degrees). Having arranged the galaxies in this order, we cut the catalog into 150 approximately equal-sized consecutive groups, which become our subcatalogs. This results in galaxies falling into the same subcatalog as most of their neighbours. (Some subcatalogs consist of multiple "islands" in different parts of the survey; we have not attempted any detailed optimization of the subcatalog cuts.)

The covariance matrix computed via the bootstrap method is noisy even as  $K \rightarrow 1$  because a finite number  $M$  of subcatalogs has been used. In the extreme case of  $M = 6N$ , the shear signals from each of the subcatalogs would form an  $M$ -dimensional plane in the  $N$ -dimensional shear space; then the signals computed from bootstrap resampling of these subcatalogs would all lie in this plane and their covariance matrix would be degenerate. As  $M$  increases, the noise in the bootstrap covariance matrix goes down, but the samples become less and less independent. We have used  $M = 150$  here. Since some of the subcatalogs receive higher weight than others (due to survey geometry, variations in source density, etc.), the calculation of Appendix D cannot be directly applied to the bootstrap method. While this makes  $\chi^2$  testing using the bootstrap method difficult, the errors on the radial-averaged intrinsic alignments obtained from  $\hat{\mathbf{C}}_{\text{boot}}$  are stable and provide a good check of the correctness of the random-lens errors.

### 4.3 Chi-squared test

We may test the random-catalog errors using a  $\chi^2$  test, since the  $\gamma_{45}$  shear must (in the mean) vanish by symmetry. At this point, it is essential to note that error covariance matrices obtained from simulations (e.g., as used in this paper) cannot be blindly used in place of the true covariance matrices in statistical tests, because they are obtained from a finite number of simulations and hence have a statistical error distribution themselves. In particular, when testing a  $\chi^2$  signal for consistency with zero, it is common to use the  $\chi^2$  test, based on the variable:

$$\chi^2_{(45)} = \frac{1}{45} \mathbf{C}_{(45)}^{-1} \mathbf{C}_{(45)} : \quad (36)$$

Here  $\mathbf{C}_{(45)} = (\mathbf{C}_{(45)}(r_1); \dots; \mathbf{C}_{(45)}(r_N))$  is the  $N$ -dimensional vector of shears in the  $N$  radial bins. If  $\mathbf{C}_{(45)}$  is Gaussian-distributed with covariance  $\mathbf{C}$  and mean 0, then  $\chi^2_{(45)}$  has a  $\chi^2$  distribution with  $N$  degrees of freedom. If we replace  $\mathbf{C}$  with the estimate  $\hat{\mathbf{C}}$ , the distribution of  $\chi^2$  becomes much more complicated. This distribution, while analytically intractable, is easy to compute via Monte Carlo simulations (see Appendix D), and we have used this approach for all the p-values quoted in this paper.

### Intrinsic alignments & shear calibration

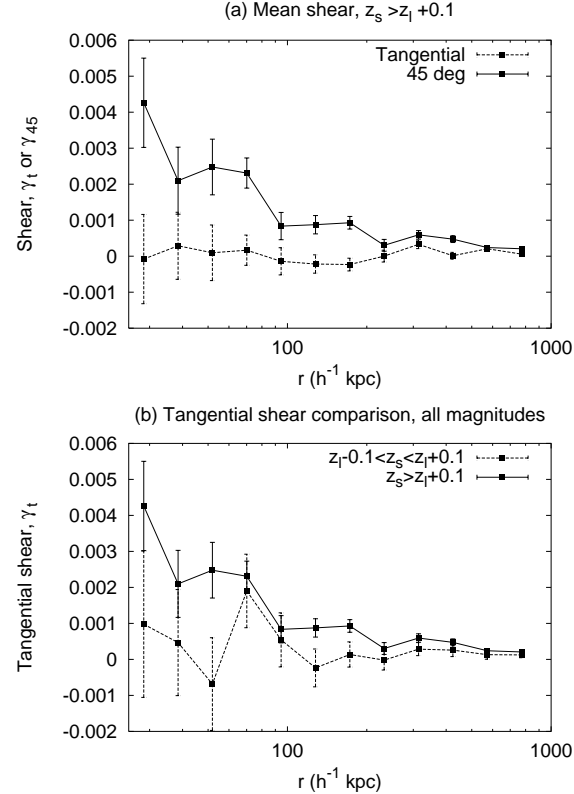


Figure 11. (a) Shear signal for  $z_s > z_l + 0.1$ . (b) Comparison of tangential shear for pairs widely separated vs. nearby in redshift. In both panels we have combined groups of three radial bins for clarity.

We test for zero  $\gamma_{45}$  by computing the statistic  $\chi^2_{(45)} = \frac{1}{45} \mathbf{C}_{\text{rand}}^{-1} \mathbf{C}_{(45)}$ , where  $\mathbf{C}_{\text{rand}}$  is the error covariance matrix derived from random catalogs. We put a "hat" on the  $\chi^2$  as a reminder that the covariance matrix is noisy, so that this statistic does not have the usual  $\chi^2$  distribution; see Appendix D. The shear data are plotted in Fig. 11(a), while the  $\chi^2_{(45)}$  values (broken down by lens luminosity) are shown in Table 3 along with their p-values (the cumulative probability of obtaining a lower  $\chi^2$  assuming that there is indeed zero signal, the errors are Gaussian, and the random realizations correctly sample the error distribution). Out of the 22 subsamples shown in the table, only 1 has a p-value for the 45-degree shear above 0.95, and 4 have p-values above 0.9. These numbers are consistent with the high p-values occurring due to chance. However, the high incidence of low p-values in the  $z_s < z_l$  samples (two subsamples have  $p_{(45)} < 0.01$ ) requires explanation. This is likely due to conservative assumptions made in computing the errors, particularly the neglect of source-lens clustering, which leads to overestimated errors and therefore lower  $\chi^2_{(45)}$  and p-values. Because source-lens clustering is more significant for the  $z_s < z_l$  samples than for the  $z_s > z_l + 0.1$  samples, this explanation is consistent with the fact that the abnormally low p-values occur for the  $z_s < z_l$  samples. Thus, we conclude that the p-values for the  $\gamma_{45}$  shear show no evidence for systematic effects and suggests that the random-catalog procedure is not detectably underestimating the error bars.

Table 3. The  $\hat{\gamma}^2$  values for  $t$  to zero shear (for both the tangential shear  $t$  and the rotated shear  $g_{12}$ ) for various lens samples. The  $p$  values quoted take into account the effect of noise on the  $\hat{\gamma}^2$  calculation as explained in Appendix D, and represent the probability of a random vector having  $\hat{\gamma}^2$  less than the given value by chance. The number of usable bins (i.e., radial bins where  $r$  is large enough to avoid overlap with the lens galaxy but small enough that the clustering contribution is unimportant) is  $N$ .

Subsample	$N$	$\hat{\gamma}^2_{(t)}$	$P_{(t)}$	$\hat{\gamma}^2_{(45)}$	$P_{(45)}$
$z_s > z_1 + 0.1$					
all	27	179.1	0.99999	70.8	0.937
$M_r > 18$	29	37.9	0.249	50.5	0.570
$19 < M_r \leq 20$	18	30	38.2	0.204	42.8
$20 < M_r \leq 21$	19	27	67.9	0.922	67.9
$21 < M_r \leq 22$	20	34	227.3	0.99998	65.9
$22 < M_r \leq 23$	21	35	160.5	0.997	57.2
$M_r < 22$	33	154.0	0.998	82.4	0.849
$z_s < z_1 + 0.1$					
all	26	39.7	0.489	27.1	0.125
$M_r > 18$	26	31.6	0.244	40.7	0.517
$19 < M_r \leq 20$	18	28	25.5	0.051	27.9
$20 < M_r \leq 21$	19	30	28.3	0.044	21.9
$21 < M_r \leq 22$	20	32	85.4	0.901	43.9
$22 < M_r \leq 23$	21	33	35.5	0.060	45.1
$M_r < 22$	30	35.1	0.142	32.6	0.097
$z_s > z_1 + 0.05$					
all	27	213	> 0.99999	75.3	0.958
$M_r > 19$	27	35.4	0.290	42.6	0.501
$21 < M_r \leq 20$	19	31	168.8	0.99990	88.2
$M_r < 21$	33	244	> 0.99999	42.7	0.157
$z_s < z_1 + 0.05$					
all	26	37.0	0.411	25.1	0.085
$M_r > 19$	26	34.6	0.331	14.2	0.002
$21 < M_r \leq 20$	19	30	35.6	0.149	28.1
$M_r < 21$	33	40.9	0.128	55.6	0.424

For completeness, we also show in Table 3 the tangential shear  $\hat{\gamma}^2_{(t)}$  and  $p$ -values. In this case, however, the signal is inconsistent with zero for many of the subsamples, with high  $p$  for the brighter luminosity lenses and widely separated ( $z_s > z_1 + 0.1$ ) lens-source pairs. As can be seen from the luminosity-averaged shear signal (Fig. 11), this is because the measured  $t > 0$  but only for widely separated pairs, consistent with gravitational lensing. Since in this paper we do not fit a model to the lensing shear signal, the tangential  $\hat{\gamma}^2_{(t)}$  values are not directly useful for establishing the accuracy of error bars.

## 5 RESULTS

### 5.1 Intrinsic shear

Table 4 shows the limits on intrinsic shear that can be computed for the various luminosity subsamples and sets of physical radii. The shear was computed by averaging the shear over the range of radii listed, weighting by the total

number of lens-source pairs in each radial bin,

$$w_i = \frac{P(N(r_i))}{\sum_i P(N(r_i))};$$

$$= \frac{N}{N_{\text{rand}}} \sum_i w_i t(r_i) = \frac{R_p}{R_p - 1} \sum_i w_i t(r_i); \quad (37)$$

where  $N$  and  $N_{\text{rand}}$  are summed over all relevant radii to account for the dilution by non-physically associated pairs. The factor of  $N = (N - N_{\text{rand}}) = R_p = (R_p - 1)$  is used because intrinsic shear only applies to the excess pairs  $N(r_i) - N_{\text{rand}}(r_i)$  (see Appendix A). This number depends on the set of radii and luminosities considered, and as can be seen from Fig. 9, is large for fainter foregrounds and for larger values of radii. (It ranges from close to 50 for the faintest subsamples, down to 1.8 for the brightest subsamples and smallest radii.) Note that shears and errors in all figures have not been corrected to account for this dilution effect, and it has no effect on the  $\hat{\gamma}^2$  values in table 3 because the dilution factor cancels out.

The errors on  $\hat{\gamma}^2$  were computed using both random catalogs and bootstrap (see Sec. 4). First, the averaged shear was computed for each of 78 random catalog outputs (using the same weighting), and  $(\text{rand})$  is the standard deviation of these averaged shears. This random catalog error was then used to compute the confidence intervals using the Student's  $t$ -distribution, which is quite close to Gaussian for 77 degrees of freedom. Second, the error from the bootstrap covariance matrices was estimated as

$$S_{(\text{boot})} = \frac{\sum_{i;j} w_i w_j C_{\text{boot},ij}}{\sum_{i;j} w_i w_j} \quad (38)$$

and confidence intervals were computed using a Gaussian distribution (since the noise in the bootstrap covariance matrix  $C_{\text{boot}}$  is unknown). In computing the confidence intervals in Table 4, we used the greater of the two errors (bootstrap or random catalog).

As a test of consistency, we compared the errors  $(\text{rand})$  and  $(\text{boot})$  computed from the random catalogs and from the bootstrap covariance matrices. For most of the samples shown in the table, the difference between the two error values was less than 25 per cent; the exceptions are the  $r < 100 h^{-1} \text{kpc}$  bins for the brighter lens samples, for which the bootstrap errors are smaller than the random catalog errors. This is probably due to the fact that the number density of source galaxies in the  $z_s < z_1 + 0.05$  samples is greater near lens galaxies than in the field, hence the shape noise is suppressed. This effect is taken into account by the bootstrap but not by the random catalogs, hence the bootstrap errors are smaller.

A possible source of contamination to the intrinsic alignment signal is gravitational lensing of source galaxies at  $z_s > z_1$ . We have attempted to estimate the magnitude of such contamination ( $10^3 g_{12}$  in the table) according to the following procedure. First, the mean value of the inverse critical surface density  $c^{-1}(z_s; z_1)$  for each sample was computed, where  $c^{-1} = 0$  for  $z_s < z_1$ . Then, the averaged shear value for the radii of interest was computed. The estimated contamination is then

$$g_{12} = \frac{\frac{c^{-1} [z_s < z_1 + 0.05]}{c^{-1} [z_s > z_1 + 0.05]} \frac{N}{N_{\text{rand}}}}{[z_s > z_1 + 0.05]};$$

Table 4. Limits on the tangential intrinsic shear  $g_1$  for various subsamples and ranges of radii (statistical errors only). The  $10^3$  column shows the central (most favored) value. Quantities have been corrected to account for dilution by non-physically associated galaxies in the  $z_s < z_l$  samples as described in the text. The statistical uncertainties ( $1\sigma$ ) on  $g_1$  are shown in the next two columns for the random-catalog and bootstrap methods.  $g_1$  is the estimated value of shear for these samples assuming a simple model for contamination by pairs that are actually gravitationally lensed (the errors are 1  $\sigma$  statistical errors on shear measurement only, i.e. they do not include uncertainties associated with the source redshift distribution). The next two columns show the pair ratios  $R_p$  for the  $z_s < z_l$  ("in") and  $z_s > z_l$  ("out") samples. Finally, we show confidence intervals for  $g_1$ . The  $95\% \text{ stat.}$  confidence interval is computed using the central value of  $g_1$  and statistical errors only. The  $99.9\% \text{ stat.+sys.}$  includes identified systematics as discussed in the text. In the row containing the  $[1;+1]$  confidence interval, we find no detection of physically associated lens-source pairs when the allowed range of systematic errors is taken into account.

Subsample	r	$10^3$	$10^3$	$(\sigma)$	$10^3$	$g_1$	$R_p$ [in]	$R_p$ [out]	confidence interval			
									95% stat.	99.9% stat.+sys.	m in	m ax
$= 0.1$												
all	[30;446]	1.6	1.0	1.0	1.45	0.17	1.155	1.008	1.8	2.1	6.2	6.6
all	[30;100]	2.7	2.1	1.7	1.96	0.32	1.355	1.007	3.4	5.0	10.5	12.5
all	[100;300]	0.4	1.1	1.3	1.26	0.22	1.181	1.010	4.1	0.8	9.5	5.1
all	[300;446]	3.6	1.7	1.6	1.58	0.25	1.120	1.007	1.4	5.4	7.4	12.8
$M_r > 18$	[30;446]	19.6	14.9	17.7	0.19	3.05	1.022	0.991	54.2	15.3	612.4	305.5
$M_r > 18$	[30;100]	18.1	25.4	22.9	9.16	4.20	1.068	0.990	77.7	23.3	206.6	115.3
$M_r > 18$	[100;300]	24.0	24.6	21.4	3.13	4.34	1.024	0.991	69.8	28.1	412.1	243.1
$M_r > 18$	[300;446]	15.5	24.0	31.4	0.25	5.02	1.017	0.990	76.7	46.3	1	1
19 to 18	[27;493]	0.7	3.3	3.7	1.52	0.59	1.079	1.013	9.5	5.1	28.6	20.8
19 to 18	[27;100]	17.5	9.5	10.0	0.11	1.56	1.148	1.010	37.3	2.1	70.2	21.5
19 to 18	[100;300]	6.9	5.4	5.2	1.26	0.88	1.094	1.014	18.8	2.5	47.6	19.6
19 to 18	[300;493]	6.1	5.0	5.3	1.89	0.86	1.068	1.013	6.1	14.6	29.0	45.3
20 to 19	[33;545]	1.1	1.8	1.6	1.53	0.33	1.119	1.004	4.1	3.3	10.8	9.7
20 to 19	[33;100]	6.2	5.2	4.8	1.56	0.78	1.248	1.002	5.8	15.1	18.4	29.8
20 to 19	[100;300]	0.7	2.6	2.4	1.28	0.49	1.149	1.007	7.1	3.1	15.9	10.7
20 to 19	[300;545]	1.6	2.4	2.3	1.67	0.45	1.102	1.004	4.8	4.7	12.9	12.8
21 to 20	[27;735]	2.6	1.3	1.3	1.18	0.20	1.139	1.011	1.1	3.9	5.8	9.8
21 to 20	[27;100]	6.6	3.5	2.6	2.59	0.57	1.427	1.007	3.0	11.0	13.2	23.2
21 to 20	[100;300]	1.0	2.0	1.8	1.32	0.28	1.217	1.014	6.2	1.6	14.1	7.8
21 to 20	[300;735]	3.5	1.5	1.6	1.08	0.26	1.119	1.010	0.8	5.6	5.8	12.7
22 to 21	[33;992]	2.8	1.1	1.2	1.57	0.21	1.146	1.006	1.1	3.6	5.7	8.8
22 to 21	[33;100]	3.6	3.3	2.3	1.80	0.54	1.807	1.027	4.8	8.5	14.4	19.0
22 to 21	[100;300]	3.3	1.8	1.8	2.00	0.37	1.355	1.019	2.2	4.8	8.9	12.4
22 to 21	[300;992]	2.6	1.4	1.6	1.48	0.26	1.121	1.005	2.0	4.1	7.2	10.1
$M_r < 22$	[45;992]	5.3	1.6	1.5	2.25	0.37	1.309	1.048	0.2	6.4	7.8	18.0
$M_r < 22$	[45;100]	0.6	6.7	3.9	4.59	1.28	2.818	1.204	18.4	8.0	43.7	29.8
$M_r < 22$	[100;300]	3.5	2.8	2.2	2.29	0.53	1.855	1.101	4.4	6.9	15.3	18.8
$M_r < 22$	[300;992]	6.3	1.9	1.8	2.28	0.44	1.246	1.042	0.2	7.8	8.2	22.1
$= 0.05$												
all	[30;446]	0.1	0.9	1.2	0.61	0.08	1.201	1.014	2.9	1.6	7.1	5.1
all	[30;100]	0.7	2.4	1.8	0.97	0.15	1.458	1.022	6.4	3.0	14.1	9.7
all	[100;300]	1.3	1.2	1.4	0.50	0.10	1.234	1.017	4.6	0.9	9.6	4.5
all	[300;446]	1.5	1.6	1.9	0.68	0.11	1.155	1.012	2.9	4.4	8.5	10.7
$M_r > 19$	[30;446]	4.5	4.1	4.8	0.51	0.32	1.067	1.004	14.5	4.4	29.9	15.8
$M_r > 19$	[30;100]	12.2	10.6	9.0	0.87	0.65	1.135	1.005	34.2	8.0	65.4	31.2
$M_r > 19$	[100;300]	8.4	5.5	5.7	0.00	0.45	1.076	1.006	19.6	2.8	38.5	14.7
$M_r > 19$	[300;446]	1.0	6.8	7.8	0.96	0.54	1.055	1.004	15.2	15.3	36.9	36.9
21 to 19	[25;545]	0.4	1.2	1.1	0.58	0.08	1.196	1.015	3.3	1.4	7.7	5.1
21 to 19	[25;100]	0.8	3.0	2.6	1.14	0.21	1.469	1.018	7.8	4.0	17.0	12.2
21 to 19	[100;300]	2.4	1.5	1.6	0.50	0.12	1.249	1.018	6.0	0.3	12.0	4.0
21 to 19	[300;545]	0.9	1.7	1.7	0.57	0.11	1.163	1.013	3.1	3.7	8.7	9.6
$M_r < 21$	[33;992]	2.3	1.0	1.0	0.61	0.07	1.253	1.018	0.4	3.7	3.4	8.0
$M_r < 21$	[33;100]	2.0	3.8	2.1	1.00	0.24	2.365	1.100	6.5	8.5	16.8	19.5
$M_r < 21$	[100;300]	2.8	1.7	1.4	0.85	0.13	1.614	1.049	1.4	5.3	6.3	11.6
$M_r < 21$	[300;992]	2.1	1.3	1.2	0.58	0.08	1.209	1.015	1.0	4.1	4.7	9.0

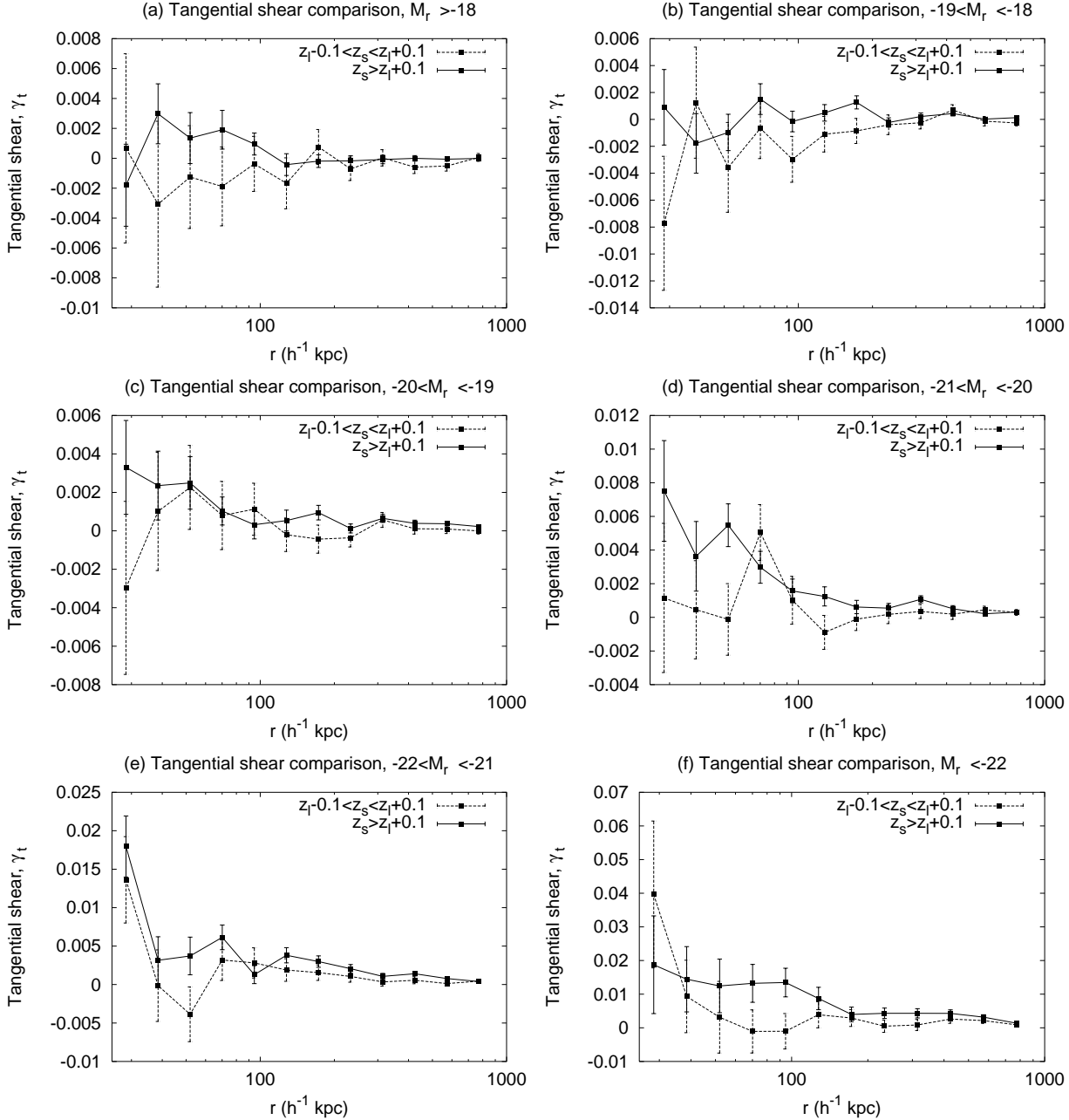


Figure 12. Shear as a function of radial pair separation; panels (a)–(f) show the six luminosity bins in order of increasing luminosity. The solid line shows the widely-separated lens-source pairs ( $z_s - z_l > 0.1$ ) and the dashed line shows the nearby pairs ( $z_s - z_l < 0.1$ ). Each point on the plot shows three of our radial bins averaged together to increase the signal/noise ratio for visual inspection.

(39)

where  $N = (N - N_{\text{rand}})$  is the dilution factor mentioned previously for the  $z_s - z_l < 0$  samples. The value  $g_1$  should thus be subtracted from  $\gamma$  in order to yield the correct intrinsic shear. While this calculation gives an estimate of the shear signal due to contamination by lensed pairs, it does not take into account the (currently unknown) photometric redshift error distribution. In particular,  $\langle z_s - z_l \rangle$  is close to zero because the lens-source separation is small, and hence its fractional systematic error may be large (possibly of order unity).

The central values of the confidence intervals in Ta-

ble 4 labeled "95% stat." are computed by subtracting the estimated gravitational lensing contamination from the observed intrinsic alignment signal ( $\gamma - g_1$ ). The statistical error on  $g_1$  is negligible and has not been included.

The "99.9% stat.+sys." confidence interval includes, in addition to statistical errors, three of the possible systematic errors: calibration biases in the shear measurement (Sec. 3.2), errors in the "correction factor"  $R_p = (R_p - 1)$  of Eq. (37) caused by seeing-induced correlations between high- and low-redshift galaxies (see Sec. 3.3.2), and systematic errors in  $g_1$  (the statistical errors are negligible). The former is taken into account by dividing the com-

puted shear by a worst-case calibration factor of 0.82 (appropriate if  $\gamma_1 = 0.18$ ). The latter is taken into account by assigning to  $R_p$  a possible systematic error equal to  $2R_p$  [but]  $\leq 1$  where  $R_p$  [but] is the pair ratio for the  $z_s > z_l + 1$  sample. This is appropriate since  $R_p$  [but] = 1 in the absence of magnification bias, photometric redshift errors, and seeing-induced systematics; it may even be a conservative estimate of seeing-induced systematics because some of the  $R_p$  [but]  $> 1$  signal observed for brighter subsamples is likely due to photometric redshift errors. Since the weakest constraints are always obtained from the smallest  $R_p$ , we replace  $R_p$  in Eq. (37) with  $R_p = 2R_p$  [but]  $\leq 1$ . (In the outermost radial bin for the  $M_r > 18$  luminosity subsample, this 'minimum value' of  $R_p$  is less than one, i.e. when systematic errors are taken into account we do not have a firm detection of clustering of source galaxies around this sample of lenses.) Finally, we allow  $\gamma_1$  to range from zero to twice the measured value, i.e. the 'maximum' value of the confidence interval for  $\gamma_1$  is computed assuming no gravitational lensing contamination at all, and the 'minimum' value is computed by subtracting  $2\gamma_1$  instead of only  $\gamma_1$  from  $\gamma_1^*$ .

As can be seen from Table 4, we find no evidence for intrinsic alignment of the satellite galaxies (there is a 'detection' at 95 per cent confidence for the  $M_r < 22$  subsample at  $45 < r < 100 h^{-1} \text{ kpc}$ , but given the large number of subsamples investigated this should not be taken as evidence for  $\gamma_1 \neq 0$ ). With all samples averaged together, we find conservatively that  $0.0062 < \gamma_1 < +0.0066$ , although we cannot exclude the possibility of a large intrinsic alignment if present around only the faintest 'lens' galaxies.

## 5.2 Systematic shear

Table 5 includes limits on the systematic shear, i.e. the additive bias contributed by observational systematics to the total shear. Such a contribution could arise if, e.g. there were a correlation between the PSF and the survey boundaries. These limits were computed by taking the average value of the shears computed from the 78 random catalogs, and finding confidence intervals around this average using the Student's t-distribution with 77 degrees of freedom (dividing by 78 because the measurement was done with 78 random catalogs). As shown, the systematic shear is consistent with zero for all samples; furthermore it is negligible compared to the statistical error in  $\gamma_1$ , as can be seen by comparing the upper limits in Table 5 to the statistical errors shown in Table 4. A plot of the systematic shear is shown in Fig. 13.

## 6 DISCUSSION

In this paper, we have set stringent new limits on intrinsic alignments as a contaminant of the galaxy-galaxy lensing signal. For example, averaging together all lens galaxies at radii out to  $446 h^{-1} \text{ kpc}$  we derive  $0.0062 < \gamma_1 < +0.0066$  (99.9 per cent confidence including identified systematics; see Table 4) or  $0.0018 < \gamma_1 < +0.0021$  (95 per cent confidence, statistical errors only). The statistical constraint is a factor of 5 (1.5 for our more conservative error bar) tighter than  $\gamma_1 = 0.01$  (95 per cent confidence) as obtained from APM/2dF data by Bernstein & Norberg (2002). It also

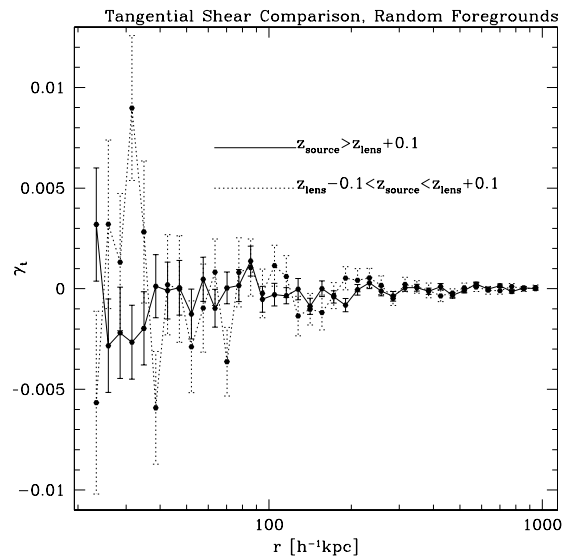


Figure 13. The tangential shear signal computed around one of the random lens catalogs.

extends to smaller radii than the measurements of nearby spirals by Lee & Pen (2001). Furthermore, our study of the luminosity and radius dependence of the intrinsic shear is useful for weak lensing studies that divide lens galaxies into luminosity subsamples.

Our limits have been obtained by using 'lens' galaxies with spectroscopic redshifts and 'source' galaxies with photometric redshifts, a different strategy than that selected by previous observers (Lee & Pen 2001; Bernstein & Norberg 2002) who used lens-source pairs selected entirely on the basis of spectroscopic redshift information. This strategy has dramatically increased our sample size and reduced our statistical uncertainties for the brighter lenses ( $M_r < -20$ ) because these are typically at redshift  $z > 0.1$ , where most of their satellites are too faint to be targeted by SDSS spectroscopy. This method does however have disadvantages. For our fainter-luminosity lenses, the photometric-redshift source method gives very large error bars (Table 4) because there are few physically associated lens-source pairs and hence any intrinsic alignment signal will be drowned out by the large number of unassociated pairs. The use of photometrically selected pairs also comes with the caveat that the limits on  $\gamma_1$  could be contaminated by a small class of galaxies that have strong intrinsic alignments but always produce incorrect photometric redshifts. It is thus recommended that the values in Table 4 with redshift slice half-width  $\Delta z = 0.1$  be used to constrain intrinsic alignments in galaxy-galaxy lensing studies, since in this case only about 20 per cent of the physically associated source galaxies are scattered out of the sample by photometric redshift errors.

Despite the recent interest in intrinsic alignments as a contaminant of cosmic shear (i.e. shear-shear correlations), there has been comparatively little theoretical work on the density-shear correlation. Lee & Pen (2001) do provide a prediction for the density-shape correlation for spiral 'source' galaxies, which we convert (see Appendix B) to  $\gamma_1 = 0.004$  at small radii  $r < 1 h^{-1} \text{ Mpc}$ . This is marginally consistent with our results (it is within our

Table 5. Limits on systematic shear in the source catalog  $10^5$  s for various subsamples and ranges of radii. Values are quoted using the errors computed from random catalogs (rand), at 95 and 99.9 per cent confidence level, using the Student's t-distribution (with errors divided by  $\sqrt{78}$  because there are 78 measurements of systematic shear).

Subsample	$r$	$10^5$	(rand)
$M_r$	$h^{-1}$ kpc	95%	99.9%
= 0.1			
all	[30;446]	[ 3:1;2:7]	[ 5:2;4:8]
all	[30;100]	[ 4:6;20:2]	[ 13:5;29:1]
all	[100;300]	[ 5:6;1:8]	[ 8:2;4:4]
all	[300;446]	[ 3:8;4:4]	[ 6:8;7:4]
> 18	[30;446]	[ 1:5;13:1]	[ 6:7;18:3]
> 18	[30;100]	[ 13:3;59:9]	[ 39:5;86:1]
> 18	[100;300]	[ 5:2;21:2]	[ 14:6;30:6]
> 18	[300;446]	[ 6:2;11:4]	[ 12:6;17:8]
19 to 18	[27;493]	[ 6:9;3:9]	[ 10:8;7:8]
19 to 18	[27;100]	[ 14:3;40:9]	[ 34:1;60:7]
19 to 18	[100;300]	[ 9:5;11:3]	[ 16:9;18:7]
19 to 18	[300;493]	[ 11:0;3:4]	[ 16:1;8:5]
20 to 19	[33;545]	[ 5:8;3:0]	[ 9:0;6:2]
20 to 19	[33;100]	[ 21:7;25:3]	[ 38:5;42:1]
20 to 19	[100;300]	[ 10:0;5:0]	[ 15:3;10:3]
20 to 19	[300;545]	[ 6:1;3:9]	[ 9:7;7:5]
21 to 20	[27;735]	[ 4:6;2:4]	[ 7:1;4:9]
21 to 20	[27;100]	[ 17:7;29:7]	[ 34:7;46:7]
21 to 20	[100;300]	[ 11:9;3:9]	[ 17:5;9:5]
21 to 20	[300;735]	[ 4:3;2:9]	[ 6:9;5:5]
22 to 21	[33;992]	[ 2:4;3:6]	[ 4:6;5:8]
22 to 21	[33;100]	[ 32:3;34:7]	[ 56:4;58:8]
22 to 21	[100;300]	[ 20:3;0:7]	[ 27:8;8:2]
22 to 21	[300;992]	[ 1:6;5:0]	[ 4:1;7:5]
< 22	[45;992]	[ 9:7;7:7]	[ 16:0;14:0]
< 22	[45;100]	[ 120:7;72:7]	[ 190:1;142:1]
< 22	[100;300]	[ 32:7;26:3]	[ 53:9;47:5]
< 22	[300;992]	[ 8:6;8:2]	[ 14:7;14:3]
= 0.05			
all	[30;446]	[ 4:1;2:7]	[ 6:6;5:2]
all	[30;100]	[ 5:4;28:2]	[ 17:4;40:2]
all	[100;300]	[ 5:9;3:9]	[ 9:4;7:4]
all	[300;446]	[ 6:6;3:2]	[ 10:1;6:7]
> 19	[30;446]	[ 3:7;8:1]	[ 7:9;12:3]
> 19	[30;100]	[ 11:6;45:0]	[ 31:9;65:3]
> 19	[100;300]	[ 2:9;14:7]	[ 9:2;21:0]
> 19	[300;446]	[ 9:9;6:3]	[ 15:6;12:0]
21 to 19	[25;545]	[ 7:8;0:8]	[ 10:9;3:9]
21 to 19	[25;100]	[ 1:0;41:8]	[ 16:4;57:2]
21 to 19	[100;300]	[ 11:6;2:0]	[ 16:6;7:0]
21 to 19	[300;545]	[ 9:7;1:1]	[ 13:6;5:0]
< 21	[33;992]	[ 5:1;4:1]	[ 8:5;7:5]
< 21	[33;100]	[ 74:1;24:1]	[ 109:3;59:3]
< 21	[100;300]	[ 18:6;10:0]	[ 28:9;20:3]
< 21	[300;992]	[ 4:6;5:4]	[ 8:2;9:0]

more conservative confidence interval of  $0.0062 < < + 0.0066$ , although the comparison is imperfect as the model applies only to spiral sources. More generally, measurements of the density-shear correlation provide a constraint on intrinsic alignment models in addition to that provided by the shear autocorrelation measurements (Pen et al. 2000;

Brown et al. 2002). It would thus be useful to compute the predictions of other intrinsic alignment models for and determine which models agree with the intrinsic shear measurements presented here and in Bernstein & Norberg (2002).

We conclude by roughly estimating the intrinsic alignment contamination to the gravitational lensing shear,  $\langle 1 R_p^{-1} \rangle$ . For example, if our source catalog restricted to  $z_s > z_l + 0.1$  were used in a lensing study of the halos of SDSS spectroscopic galaxies, we would have a contamination fraction  $1 R_p^{-1} 0.01$  in the  $100 < r < 300 h^{-1}$  kpc bin and intrinsic alignment contamination  $j_j < 0.0095$  (see Table 4), corresponding to a contamination to the gravitational lensing shear at the level of  $< 9.5 \times 10^{-5}$ . This is approximately equal to the size of the 1 error bars at these radii for our full sample ( $1.0 \times 10^4$ ; see Fig. 11) and a factor of six less than the shear signal,  $5.8 \times 10^{-4}$ . Slightly weaker constraints are placed on the intrinsic alignments around the brighter lenses, but in these cases the lensing signal is a factor of several higher, e.g. for the  $21 > M_r > 22$  magnitude range we have  $j_j < 0.0124$  at  $100 < r < 300 h^{-1}$  kpc,  $1 R_p^{-1} 0.02$ , and shear signal  $\tau = 2 \times 10^{-3}$ , so the contamination is at worst about a factor of eight smaller than the signal. These results indicate at 99.9 per cent confidence that, except possibly for the faintest lens galaxies, intrinsic alignments are only contaminating the sub-Mpc scale galaxy-galaxy lensing signal at the  $\sim 15$  per cent level.

## ACKNOWLEDGMENTS

We acknowledge useful discussions with James Gunn, Zeljko Ivezic, Yeong-Shang Loh, Robert Lupton, Patrick McDonald, and Michael Strauss.

C.H. is supported by a NASA Graduate Student Researchers Program (GSRP) fellowship. R.M. is supported by an NSF Graduate Research Fellowship. U.S. is supported by Packard Foundation, Sloan Foundation, NASA NAG 5-1993, and NSF CAREER-0132953.

Funding for the creation and distribution of the SDSS Archive has been provided by the Alfred P. Sloan Foundation, the Participating Institutions, the National Aeronautics and Space Administration, the National Science Foundation, the U.S. Department of Energy, the Japanese Monbukagakusho, and the Max-Planck Society. The SDSS Web site is <http://www.sdss.org/>.

The SDSS is managed by the Astrophysical Research Consortium (ARC) for the Participating Institutions. The Participating Institutions are The University of Chicago, Fermilab, the Institute for Advanced Study, the Japan Participation Group, The Johns Hopkins University, Los Alamos National Laboratory, the Max-Planck-Institute for Astronomy (MPIA), the Max-Planck-Institute for Astrophysics (MPA), New Mexico State University, University of Pittsburgh, Princeton University, the United States Naval Observatory, and the University of Washington.

## REFERENCES

Abazajian K. et al. 2003, *Astron. J.*, 126, 2081

Bacon D. J., Refregier A. R., Ellis R. S., 2000, MNRAS, 318, 625

Bacon D. J., Refregier A., Colledge D., Ellis R. S., 2001, MNRAS, 325, 1065

Bartelmann M., Schneider P., 2001, Phys. Rep., 340, 291

Bernstein G. M., Jarvis M., 2002, Astron. J., 123, 583

Bernstein G. M., Norberg P., 2002, Astron. J., 124, 733

Banton M. R., Lin H., Lupton R. H., Malesy F. M., Young N., Zehavi I., Loveday J., 2003a, Astron. J., 125, 2276

Banton M. R., Brinkmann J., Csabai I., Doi M., Eisenstein D., Fukugita M., Gunn J. E., Hogg D. W., Schlegel D. J., 2003b, Astron. J., 125, 2348

Brown M. L., Taylor A. N., Hambley N. C., Dye S., 2002, MNRAS, 333, 501

Brown M. L., Taylor A. N., Bacon D. J., Gray M. E., Dye S., Misenheimer K., Wolk C., 2003, MNRAS, 335, L89

Catelan P., Kamionkowski M., Landford R. D., 2001, MNRAS, 341, 100

Budavari T., Szalay A. S., Connolly A. J., Csabai I., Dickinson M., 2000, Astron. J., 120, 1588

Catelan P., Kamionkowski M., Landford R. D., 2001, MNRAS, 320, L7

Colless M., Dalton G., Maddox S., Sutherland W., Norberg P., Cole S. et al., 2001, MNRAS, 328, 1039

Crittenden R. G., Natarajan P., Pen U., Theuns T., 2001, Astrophys. J., 559, 552

Croft R. A. C., Metzler C. A., 2000, Astrophys. J., 545, 561

Csabai I., Connolly A. J., Szalay A. S., Budavari T., 2000, Astron. J., 119, 69

Csabai I., Budavari T., Connolly A. J., Szalay A. S., Györy Z., Benitez N., Annis J., Brinkmann J., Eisenstein D., Fukugita M., Gunn J., Kent S., Lupton R., Nichol R. C., Stoughton C., 2003, Astron. J., 125, 580

Erben T., Van Waerbeke L., Bertin E., Mellier Y., Schneider P., 2001, Astron. Astrophys., 366, 717

Finkbeiner D. et al., 2004, in preparation

Fischer P., Tyson J. A., 1997, Astron. J., 114, 14

Fischer P., Mackay T. A., Sheldon E., Connolly A., Stebbins A., Frieman J. A., Jain B., Jurek M., Johnston D., Bernstein G. et al., 2000, Astron. J., 120, 1198

Fukugita M., Ichikawa T., Gunn J. E., Doi M., Shimasaku K., Schneider D. P., 1996, Astron. J., 111, 1748

Gunn J. E., Carr M., Rockosi C., Sekiguchi M., et al., 1998, Astron. J., 116, 3040

Guzik J., Seljak U., 2002, MNRAS, 335, 311

Heavens A., Refregier A., Heymans C., 2000, MNRAS, 319, 649

Heavens C., Brown M., Heavens A., Misenheimer K., Taylor A., Wolk C., 2004, MNRAS, 347, 895

Hirata C. M., Seljak U., 2003, MNRAS, 338, 343, 459

Hoekstra H., 2004, MNRAS, 347, 1337

Hoekstra H., Franx M., Kuijken K., Squires G., 1998, New Astron. Rev., 42, 137

Hoekstra H., Franx M., Kuijken K., 2000, Astrophys. J., 532, 88

Hoekstra H., Franx M., Kuijken K., Carlberg R. G., Yee H. K. C., Lin H., Morris S. L., Hall P. B., Patton D. R., Sawicki M., Wirth G. D., 2001, Astrophys. J. Lett., 548, 5

Hoekstra H., Yee H. K. C., Gladders M. D., Barrientos L. F., Hall P. B., Infante L., 2002, ApJ, 572, 55

Hogg D. W., Finkbeiner D. P., Schlegel D. J., Gunn J. E., 2001, Astron. J., 122, 2129

Hudson M. J., Gwyn S. D. J., Dahle H., Kaiser N., 1998, Astrophys. J., 503, 531

Jarvis M., Bernstein G. M., Fischer P., Smith D., Jain B., Tyson J. A., Wittman D., 2003, Astron. J., 125, 1014

Jing Y. P., 2002, MNRAS, 335, L89

Kaiser N., 2000, Astrophys. J., 537, 555

Kaiser N., Squires G., Roadhurst T., 1995, Astrophys. J., 449, 460

Lee J., Pen U., 2000, Astrophys. J. Lett., 532, L5

Lee J., Pen U., 2001, Astrophys. J., 555, 106

Lee J., Pen U., 2002, Astrophys. J. Lett., 567, L111

Luppino G. A., Kaiser N., 1997, Astrophys. J., 475, 20

Lupton R., Gunn J. E., Ivezić Z., Knapp G. R., Kent S., Yasuda N., 2001, in ASP Conf. Ser. 238, Astronomical Data Analysis Software and Systems X, ed. Hamden F. R. Jr., Primini F. A., Payne H. E. (San Francisco: Astron. Soc. Pac.), p. 269

Lupton R. et al., 2004, in preparation

Maddox S. J., Efstathiou G., Sutherland W. J., Loveday J., 1990, MNRAS, 243, 692

Mandelbaum R. et al., 2004, in preparation

Mackay T. A., Sheldon E. S., Racusin J., Fischer P., Seljak U., Stebbins A., Johnston D., Frieman J. A., Bahcall N., Brinkmann J., Csabai I., Fukugita M., Hennessy G. S., Ivezić Z., Lamb D. Q., Loveday J., Lupton R. H., Gunn J. A., Nichol R. C., Pier J. R., York D. G., 2001, astro-ph/0108013

Miralda-Escude J., 1991, Astrophys. J., 380, 1

Padmanabhan N., Seljak U., Strauss M. A., Banton M. R., Kaumann G., Schlegel D. J., Tremonti C., Bahcall N. A., Bernardi M., Brinkmann J., Fukugita M., Ivezić Z., 2004, New Astron., 9, 329

Pen U., Lee J., Seljak U., 2000, Astrophys. J. Lett., 543, L107

Pier J. R., Gunn J. A., Hindsley R. B., Hennessy G. S., Kent S. M., Lupton R. H., Ivezić Z., 2003, Astron. J., 125, 1559

Refregier A., 2003, Ann. Rev. Astron. Astrophys., 41, 645

Refregier A., 2003, MNRAS, 338, 35

Refregier A., Bacon D., 2003, MNRAS, 338, 48

Rhodes J., Refregier A., Roth E. J., 2001, ApJ, 552, L85

Schlegel D. J., Finkbeiner D. P., Davis M., 1998, Astrophys. J., 500, 525

Schlegel D. et al., 2004, in preparation

Sheldon E. S., Annis J., Bohringer H., Fischer P., Frieman J. A., Jurek M., Johnston D., Mackay T. A., Miller C., Nichol R. C., Stebbins A., Voges W., et al., 2001, Astrophys. J., 554, 881

Sheldon E. S., Johnston D. E., Frieman J. A., Scranton R., Mackay T., Connolly A. J., Budavari T., Zehavi I., Bahcall N., Brinkmann J., Fukugita M., 2003, astro-ph/0312036, Astron. J., accepted

Smith D. R., Bernstein G. M., Fischer P., Jarvis M., 2001, Astrophys. J., 551, 643

Smith J. A., Tucker D. L., Kent S., Rich mond M. W., Fukugita M., Ichikawa T., Ichikawa S., Jorgensen A. M.,

Uomoto A., Gunn J. E., Hamabe M., Watanabe M., Tolea A., Henden A., Annis J., Pier J. R., McKay T. A., Brinkmann J., Chen B., Holtzman J., Shimashaku K., York D. G., 2002, *Astron. J.*, 123, 2121

Spergel D. N., Verde L., Peiris H. V., Komatsu E., Nolta M. R., Bennett C. L., Halpern M., Hinshaw G., Jarosik N., Kogut A., Limon M., Meyer S. S., Page L., Tucker G. S., Weiland J. L., Wollack E., Wright E. L., 2003, *Astrophys. J. Suppl.*, 148, 175

Stoughton C., Lupton R. H., et al., 2002, *Astron. J.*, 123, 485

Strauss M. A., Weinberg D. H., Lupton R. H., Narayanan V. K., et al., 2002, *Astron. J.*, 124, 1810

Van den Bosch F. C., Abel T., Croft R. A. C., Hernquist L., White S. D. M., 2002, *Astrophys. J.*, 576, 21

Van Waerbeke L., Mellier Y., Erben T., Cuillandre J. C., Bernardeau F., Maoli R., Bertin E., McCracken H. J., Le Fevre O., Fort B., Dantel-Fort M., Jain B., Schneider P., 2000, *Astron. Astrophys.*, 358, 30

Van Waerbeke L., Mellier Y., Pello R., Pen U.-L., McCracken H. J., Jain B., 2002, *Astron. Astrophys.*, 393, 369

York D. G., et al., 2000, *Astron. J.*, 120, 1579

#### APPENDIX A : INTRINSIC SHEAR AND CORRELATION FUNCTION

In principle, the tangential component of intrinsic shear  $\hat{\gamma}_t$  is a function not only of the transverse separation  $r$  between the lens and source galaxy, but also on the line-of-sight separation  $u$ . The contribution of the intrinsic alignments to the shear  $\hat{\gamma}_t$  observed in galaxy-galaxy weak lensing is:

$$\hat{\gamma}_t(\text{intr}; r) = \frac{\int_{-R}^R \gamma_t(r; u) n(r; u) du}{\int_{-R}^R n(r; u) du}; \quad (\text{A } 1)$$

where  $n(r; u) du/d^2 r$  is the number of sources with line-of-sight separation between  $u$  and  $u + du$  in area  $d^2 r$  in the lens plane. This contamination is typically estimated by comparing the total number of sources observed per unit area in the lens plane, i.e.  $\int_{-R}^R n(r; u) du$ , to the number of sources observed in a randomly selected field,  $\int_{-R}^R n(1; u) du$ . We express this in terms of a 'pair ratio'  $R_p(r)$ :

$$R_p(r) = \frac{\int_{-R}^R n(r; u) du}{\int_{-R}^R n(1; u) du}; \quad (\text{A } 2)$$

The simplest interpretation of the pair ratio is that the fraction of the source galaxies that are physically unassociated with the lens is  $R_p^{-1}$ , and that the remaining fraction  $1 - R_p^{-1}$  are physically associated with the lens. This motivates the definition of the projected intrinsic shear  $\gamma_t(r)$  of physically associated galaxies as:

$$\gamma_t(r) = \frac{\hat{\gamma}_t(\text{intr}; r)}{1 - R_p^{-1}}; \quad (\text{A } 3)$$

Most analyses of the effect of intrinsic alignments on galaxy-galaxy lensing studies (e.g. Bernstein & Norberg 2002; Sheldon et al. 2003) have used Eq. (A 3) to compute  $\hat{\gamma}_t(\text{intr})$  from the measured pair ratio  $R_p$  and an estimate of the intrinsic shear of physically associated galaxies  $\gamma_t(r)$  based

on spectroscopically selected lens-source pairs at the same redshift.

While Eq. (A 3) is directly useful for measuring the intrinsic alignment and estimating the contamination of weak lensing results, we can also write  $\gamma_t(r)$  in terms of a projection integral along the line of sight. Substituting Eqs. (A 1) and (A 2) into Eq. (A 3), we find:

$$\gamma_t(r) = \frac{\int_{-R}^R \gamma_t(r; u) n(r; u) du}{\int_{-R}^R n(1; u) du}; \quad (\text{A } 4)$$

The integrands in both the numerator and denominator of Eq. (A 4) vanish at large  $|u|$  (so long as the magnification bias due to gravitational lensing is small). At small  $|u|$  (i.e. much less than the typical distance to the lenses, so that variations in  $n(1; u)$  can be ignored),  $n(r; u)$  is related to the galaxy-galaxy correlation function via  $n(r; u) / (1 + \frac{P}{r^2 + u^2})$ . Therefore we may write

$$\gamma_t(r) = \frac{\int_{-R}^R \gamma_t(r; u) [1 + \frac{P}{r^2 + u^2}] du}{\int_{-R}^R \frac{P}{r^2 + u^2} du}; \quad (\text{A } 5)$$

which is the relation of  $\gamma_t(r)$  to fundamental (as opposed to observed) quantities.

#### APPENDIX B : RELATION OF INTRINSIC SHEAR TO POSITION ANGLE STATISTICS

Lee & Pen (2000) and Lee & Pen (2001) measure density-shape correlations using the position angle statistic,

$$\beta_{2D}(r_{3D}) = \text{hcos}^2 i - \frac{1}{2} = \frac{1}{2} \text{hcos}^2 i; \quad (\text{B } 1)$$

where  $i$  is the position angle of the source galaxy's minor axis relative to the lens (0 indicates radial alignment,  $\pi/2$  tangential alignment) and the three-dimensional pair separation is  $r_{3D} = \sqrt{r^2 + u^2}$ . Lee & Pen (2001) consider spiral galaxies and hence interpret the minor axis as the (projected) rotation axis of the galaxy, but Eq. (B 1) is what is directly measured.

We consider here a crude model for the conversion between  $\beta_{2D}$  and the intrinsic shear  $\gamma_t$ . Formulas for the transformation of ellipticity under shear are given by Miralda-Escude (1991); using that  $\tan 2\theta = e_{45} - e_t$  (in a coordinate system aligned with the direction to the lens galaxy) we can find the transformation of the position angle under shear,

$$\frac{\partial \theta}{\partial \gamma_t} = e^{-1} \sin 2\theta; \quad (\text{B } 2)$$

Substitution into Eq. (B 1) yields

$$\frac{d\beta_{2D}}{d\gamma_t} = \frac{1}{2} e^{-1} \sin 2\theta \frac{d}{d\theta} \cos 2\theta = \frac{1}{2} \text{h} e^{-1} i; \quad (\text{B } 3)$$

We define this quantity to be the position angle responsivity  $R_\beta$ ; for our  $r < 19$  galaxies (with negligible measurement noise in the ellipticity),  $\text{h}^{-1} i = 2.75$  and  $R_\beta = 1.38$ . The theory of Lee & Pen (2001) suggests that at small radii ( $r_{3D} < 1.5 h^{-1} \text{ Mpc}$ ) we should have  $\beta_{2D}(r) = 0.0057$  for spirals (see their Fig. 2) or  $\gamma_t = \beta_{2D} = R_\beta = 0.0041$ . Since the galaxy autocorrelation function  $\langle \beta_{2D} \rangle = 1$  at these radii, we expect  $\gamma_t = 0.0041$  (cf Eq. A 5). This conversion is only a rough estimate since the relation Eq. (B 3) between

$\mathbf{J}_{2D}$  and  $\mathbf{J}_+$  was derived for a gravitational shear, and it need not be the correct relation for intrinsic shear.

Using the conversion  $R_+ = 1.38$ , the data presented in Fig. 2 of Lee & Pen (2001) correspond to  $\mathbf{J}_+ = 0.0037 \pm 0.0025$  at  $r_{3D} = 500 \text{ h}^{-1} \text{ kpc}$ .

#### APPENDIX C: NOISE-RECTIFICATION BIAS

Noise in galaxy images has several effects for weak lensing. The best-known effect is the introduction of measurement noise in the ellipticity. It has also been pointed out that noise can also couple to the PSF anisotropy to produce spurious power in cosmological shear measurements, even if the PSF correction is otherwise exact (Kaiser 2000; Bernstein & Jarvis 2002). This occurs because of a noise-rectification bias, i.e. the ellipticity is a nonlinear function of the image intensity so that an unbiased estimate of the intensity need not translate into an unbiased estimate of the ellipticity. Here we estimate the effect of noise-rectification biases on the shear calibration of low signal-to-noise ratio galaxies.

Our plan for approaching this problem is as follows:

(i) Determine, for a circular Gaussian galaxy with unit radius  $\mathbf{r} = 1$  and unit central intensity  $I(0) = 1$ , the mean and covariance of the measured adaptive moments  $\hat{M}^{(I)}$  to leading order in the noise.

(ii) Use scaling and symmetry principles to derive the mean and covariance of  $\hat{M}^{(I)}$  for a general elliptical Gaussian galaxy.

(iii) Propagate these errors to the PSF-corrected ellipticity  $\hat{\epsilon}^{(f)}$ .

Here we will neglect corrections due to non-Gaussianity of the galaxy or PSF.

We first introduce some notation. We write the normalization, centroid and moments of the galaxy as a six-dimensional vector:

$$\mathbf{c} = (A; \mathbf{x}_0; \mathbf{y}_0; M^{-1} \mathbf{j}^{xx}; M^{-1} \mathbf{j}^{xy}; M^{-1} \mathbf{j}^{yy}); \quad (C1)$$

(We could have used the matrix elements of  $M$  to parameterize the family of Gaussians instead of  $M^{-1}$ ; however using  $M^{-1}$  simplifies the algebra.) We now introduce the notation:

$$J(\mathbf{r}; \mathbf{c}) = A \exp \frac{(\mathbf{r} - \mathbf{r}_0)^T M^{-1} (\mathbf{r} - \mathbf{r}_0)}{2}; \quad (C2)$$

Thus the energy functional Eq. (1) becomes

$$E(\mathbf{c}; \mathbf{I}) = \frac{1}{2} \int \mathbf{I}(\mathbf{r}) J(\mathbf{r}; \mathbf{c})^2 d^2 \mathbf{r}; \quad (C3)$$

or, written as an inner product:

$$E(\mathbf{c}; \mathbf{I}) = \frac{1}{2} \mathbf{hI} \mathbf{J}; \mathbf{I} \mathbf{J} \mathbf{i}; \quad (C4)$$

(We suppress the  $\mathbf{c}$  argument of  $J$  for clarity.) Minimizing this yields:

$$0 = \mathbf{hI} \mathbf{J}; \mathbf{J} \mathbf{i}; \quad (C5)$$

where  $\mathbf{J} = \mathbf{J}^T = \mathbf{c}$ .

We may obtain the dependence of  $\mathbf{c}$  on  $\mathbf{I}$  by taking the functional derivative of Eq. (C5) with respect to  $I(r_i)$ :

$$0 = \mathbf{J}(r_1) + (\mathbf{hI} \mathbf{J}; \mathbf{J} \mathbf{i} \mathbf{hJ}; \mathbf{J} \mathbf{i}) \frac{dc}{I(n)}; \quad (C6)$$

The second derivative of Eq. (C5) is more complicated; for the particular case  $\mathbf{I} = \mathbf{J}$ , it is:

$$\begin{aligned} 0 = & \frac{d^2 c}{I(n) I(r_2)} (\mathbf{hJ} \mathbf{J}; \mathbf{I} \mathbf{J} \mathbf{i} \mathbf{hJ}; \mathbf{J} \mathbf{i}) \\ & \frac{dc}{I(n)} \frac{dc}{I(r_2)} \mathbf{hJ} \mathbf{J}; \mathbf{J} \mathbf{i} + \mathbf{hJ} \mathbf{J}; \mathbf{J} \mathbf{i} \\ & + \mathbf{hJ} \mathbf{J}; \mathbf{J} \mathbf{i} \mathbf{hJ} \mathbf{J}; \mathbf{I} \mathbf{J} \mathbf{i} \\ & + \frac{dc}{I(n)} \mathbf{J}(r_2) + \frac{dc}{I(r_2)} \mathbf{J}(r_1); \end{aligned} \quad (C7)$$

Defining  $\mathbf{H}$  to be the matrix inverse of  $\mathbf{H}^{-1} = \mathbf{hJ} \mathbf{J}; \mathbf{J} \mathbf{i}$ , and evaluating the derivatives at  $\mathbf{I} = \mathbf{J}$ , gives

$$\frac{dc}{I(r)} \Big|_{\mathbf{I}=\mathbf{J}} = \mathbf{H} \mathbf{J}(r) \quad (C8)$$

and

$$\frac{d^2 c}{I(r) I(r)} \Big|_{\mathbf{I}=\mathbf{J}} d^2 \mathbf{r} = \mathbf{H} \mathbf{H} \mathbf{hJ}; \mathbf{J} \mathbf{i}; \quad (C9)$$

In Eq. (C9) we have only computed the trace of the second derivative matrix; this is all we will need.

A circular Gaussian galaxy with unit radius and central intensity has measured profile:

$$\hat{J}(\mathbf{r}) = e^{-(x^2 + y^2)/2} + \epsilon(\mathbf{r}) = J(\mathbf{r}; \mathbf{C}) + \epsilon(\mathbf{r}); \quad (C10)$$

where  $\epsilon$  is the noise and  $\mathbf{C} = (1; 0; 0; 1; 0; 1)$  are the moments of the galaxy (in the absence of noise). The noise is assumed to be white:

$$\mathbf{h}(\mathbf{r}_1) \mathbf{J}(\mathbf{r}_2) \mathbf{i} = N \mathbf{h}^{(2)}(\mathbf{r}_1 \mathbf{r}_2); \quad (C11)$$

The mean and covariance of the measured moments  $\hat{\mathbf{c}}$  can then be determined to order  $O(N)$  from the equations:

$$\mathbf{h} \hat{\mathbf{c}} \mathbf{i} = \mathbf{C} + \frac{1}{2} N \frac{d^2 c}{I(r) I(r)} \Big|_{\mathbf{I}=\mathbf{J}} d^2 \mathbf{r}; \quad (C12)$$

and:

$$\text{Cov}(\hat{\mathbf{c}}; \hat{\mathbf{c}}) = N \frac{dc}{I(r)} \frac{dc}{I(r)} \Big|_{\mathbf{I}=\mathbf{J}} d^2 \mathbf{r}; \quad (C13)$$

Substituting Eqs. (C8) and (C9) yields:

$$\mathbf{h} \hat{\mathbf{c}} \mathbf{i} = \mathbf{C} + \frac{1}{2} N \mathbf{H} \mathbf{H} \mathbf{hJ}; \mathbf{J} \mathbf{i} \mathbf{J}(\mathbf{r}) \mathbf{J}(\mathbf{r}) d^2 \mathbf{r} \quad (C14)$$

and

$$\text{Cov}(\hat{\mathbf{c}}; \hat{\mathbf{c}}) = N \mathbf{H} \mathbf{H} \mathbf{i}; \quad (C15)$$

The substitution of the particular functional form Eq. (C2) into Eqs. (C14) and (C15) is a straightforward but lengthy exercise. The  $\mathbf{H}$  matrix in the basis of Eq. (C1) is

$$\mathbf{H} = \frac{2}{\pi} \begin{bmatrix} 0 & 1 & 0 & 0 & 1 & 1 \\ 1 & 0 & 0 & 0 & 0 & 0 \\ 0 & 0 & 1 & 0 & 0 & 0 \\ 0 & 0 & 0 & 4 & 0 & 0 \\ 1 & 0 & 0 & 0 & 0 & 0 \\ 0 & 0 & 0 & 0 & 2 & 0 \end{bmatrix}; \quad (C16)$$

and the product  $\mathbf{H} \mathbf{J}(\mathbf{r})$  appearing in Eq. (C14) is

$$\mathbf{H} \mathbf{J}(\mathbf{r}) = \frac{2}{\pi} \begin{bmatrix} 4 & 2 \end{bmatrix} e^{-r^2/2}; \quad (C17)$$

From this we find that the mean values of the entries in  $M^{(1)}$  are

$$h\hat{M}^{(1)}_{xx}i = h\hat{M}^{(1)}_{yy}i = 1 + \frac{8}{N}; \quad (C18)$$

and  $h\hat{M}^{(1)}_{xy}i = 0$ . Using the Taylor series for the moments:

$$\hat{M} = 1 - \hat{M}^{(1)} - \hat{M}^{(1)}_1 + \hat{M}^{(1)}_1 - \hat{M}^{(1)}_2 + O(\hat{M}^{(1)}_1 - \hat{M}^{(1)}_2); \quad (C19)$$

we can find the mean of  $\hat{M}$  to be

$$h\hat{M}_{ij}i = 1 + \frac{4}{N} \hat{M}_{ij}; \quad (C20)$$

and the covariance to be:

$$\text{Cov}(\hat{M}_{ij}; \hat{M}_{kl}) = \frac{4}{N} (\hat{M}_{ik} \hat{M}_{jl} + \hat{M}_{il} \hat{M}_{jk}); \quad (C21)$$

We now generalize Eqs. (C20) and (C21). Clearly the energy functional is translation-invariant, so Eqs. (C20, C21) cannot depend on  $r_0$ . If the amplitude  $A$  is increased by some factor, and the noise amplitude  $N$  is similarly increased, the energy minimization remains unchanged, so the result can depend on  $A$  and  $N$  only through the ratio  $A = N$ . The problem is also invariant under linear transformations of  $r$ , so that if  $M$  is changed, and  $N$  is increased by the factor  $\det M$  (to account for the delta function in Eq. C11 and the change of measure in the integration over  $d^2r$ ), then the linear transformation acts simply on Eqs. (C20, C21). We have concluded that the generalizations of Eqs. (C20, C21) are

$$h\hat{M}_{ij}i = 1 + 4 \frac{N}{A^2 \det M} M_{ij} \quad (C22)$$

and

$$\text{Cov}(\hat{M}_{ij}; \hat{M}_{kl}) = 4 \frac{N}{A^2 \det M} (M_{ik} M_{jl} + M_{il} M_{jk}); \quad (C23)$$

The quantity  $N = A^2 \det M$  is recognized as  $\frac{P}{\sigma^2}$ , where  $P$  is the signal-to-noise ratio for detection of the galaxy in an adaptive elliptical Gaussian filter (Bernstein & Jarvis 2002).

We have reached the final stage in our plan, namely to translate the errors in  $M$  into the calibration bias of the ellipticity estimator. We consider here only the simplest case, that of a circular Gaussian PSF and an elliptical Gaussian galaxy with its major axis aligned along the  $x$ -axis. The estimated ellipticity is:

$$\hat{e}_+^{(f)} = \frac{\hat{Q}^{(1)}}{\hat{T}^{(1)} - T^{(P)}}, \quad (C24)$$

where  $T$  is the trace and  $Q = M_{xx} - M_{yy}$  is the quadrupole moment. The effects of the bias (Eq. C22) and noise (Eq. C23) in  $M^{(1)}$  can be determined from the first and second derivatives (respectively) of  $\hat{e}_+^{(f)}$  with respect to  $M^{(1)}$ ; the order  $O(N)$  terms are:

$$\begin{aligned} h\hat{e}_+^{(f)}i &= e_+^{(f)} + \frac{h\hat{Q}^{(1)}i}{T^{(1)} - T^{(P)}} - \frac{Q^{(1)}h\hat{T}^{(1)}i}{(T^{(1)} - T^{(P)})^2} \\ &\quad \text{Cov}(\hat{Q}^{(1)}; \hat{T}^{(1)}) + \frac{Q^{(1)}h(\hat{T}^{(1)})^2i}{(T^{(1)} - T^{(P)})^3}; \end{aligned} \quad (C25)$$

where we have used the bias  $h\hat{Q}^{(1)}i = h\hat{T}^{(1)}i - Q$ . For a galaxy with only ellipticity (i.e. position angle along the  $x$ - or  $y$ -axis), the biases and covariances obtained from

Eqs. (C22, C23) are:

$$\begin{aligned} h\hat{Q}^{(1)}i &= 4 \frac{2T^{(1)}e_+^{(1)}}{}; \\ h\hat{T}^{(1)}i &= 4 \frac{2T^{(1)}}{}; \\ h(\hat{T}^{(1)})^2i &= 4 \frac{2T^{(1)}(1 + e_+^{(1)})^2}{}; \\ \text{Cov}(\hat{Q}^{(1)}; \hat{T}^{(1)}) &= 8 \frac{2T^{(1)}e_+^{(1)}}{}; \\ h(\hat{Q}^{(1)})^2i &= 4 \frac{2T^{(1)}(1 + e_+^{(1)})^2}{}; \end{aligned} \quad (C26)$$

This leads us to the result for the change in ellipticity calibration:

$$\frac{h\hat{e}_+^{(f)}i}{e_+^{(f)}} = \frac{4}{2} (1 - 3R_2^{-1} + R_2^{-2} + e_+^{(f)2}); \quad (C27)$$

We have verified Eqs. (C22), (C23), and (C27) in "toy" simulations.

We have used this result as an approximation to the shear calibration  $\hat{e}_+^{(f)}$ , although this is not exact because the shear calibration is determined by the derivative of  $h\hat{e}_+^{(f)}i$  with respect to  $e_+^{(f)}$ , which is not exactly equal to the ratio  $h\hat{e}_+^{(f)}i/e_+^{(f)}$  when the latter is not constant. The calibration bias obtained from Eq. (C27) is shown in Fig. 6.

#### APPENDIX D : CHI-SQUARED TEST WITH ERRORS FROM SIMULATIONS

We perform several tests for consistency with zero signal using a  $\chi^2$  test. Since we have derived our covariance matrix from simulations, we must also take into account the noise from only having a finite number of simulations.

If we have estimated a shear in  $N$  radial bins, we can construct an  $N$ -dimensional shear vector  $\mathbf{x}$ . The  $M$  simulations provide us with  $M$  simulated shear vectors  $\mathbf{x}^{(1)} \mathbf{x}^{(2)} \dots \mathbf{x}^{(M)}$  from which we can compute the sample covariance  $\hat{C}$  (see Eq. 33). We are interested in the distribution of the variable  $\chi^2 = \mathbf{x}^T \hat{C}^{-1} \mathbf{x}$  (D1)

under the null hypothesis that  $\mathbf{x}$  is Gaussian with mean 0 and the same covariance  $C$  as the simulated shear vectors.

In order to determine the distribution of  $\chi^2$  via Monte Carlo, we define the vectors  $\mathbf{x}^{(1)} = C^{-1/2} \mathbf{x}^{(1)}$  and  $\mathbf{x}^{(2)} = C^{-1/2} \mathbf{x}^{(2)}$ . (Here the symmetric matrix  $C^{-1/2}$  has the same eigenvectors as  $C$  but the eigenvalues  $\lambda_i$  are replaced by  $\lambda_i^{1/2}$ .) Then we find:

$$\chi^2 = \mathbf{x}^T D^{-1} \mathbf{x}; \quad (D2)$$

where the matrix  $D$  is given by:

$$D = \frac{1}{M-1} \mathbf{x}^{(1)} \mathbf{x}^{(1)T} \mathbf{x}^{(2)} \mathbf{x}^{(2)T} \quad (D3)$$

Here  $\mathbf{x}_i$  are the sample means of the  $\mathbf{x}^{(1)}$ . Since the  $\mathbf{x}_i$  and  $\mathbf{x}_i^{(2)}$  are independent Gaussians of zero mean and unit variance, it is computationally easy to generate sample from Eq. (D3), so we can use a Monte Carlo method to compute the probability distribution for  $\chi^2$ .

As  $M \rightarrow 1$  (with  $N$  fixed),  $D \rightarrow 1$  and the distribution of  $\chi^2$  converges to the  $\chi^2$  distribution. However, the convergence is not rapid. To see this, we note that by Wicksell's theorem,  $D$  has expectation value equal to the identity 1 and covariance:

$$h(D_{ij} - \bar{D}_{ij}) D_{kl} - \bar{D}_{kl} \bar{D}_{ij} = \frac{i_k j_l + i_l j_k}{M} - 1; \quad (D 4)$$

Using the Taylor series for the inverse of a matrix, and the fact that the higher-order moments of the  $D$  distribution decrease as  $M^{-2}$  or faster, we find the asymptotic expansion:

$$hD^{-1}i = 1 + hD^{-1}i + O(M^{-2}); \quad (D 5)$$

Since  $x$  is independent of  $D$ :

$$h^2 i = N + \frac{N(N+1)}{M} + O(M^{-2}); \quad (D 6)$$

which is found to agree with the mean obtained via Monte Carlo. Since the standard deviation of the  $\chi^2$  distribution is  $\sqrt{2N}$ , we must take  $M = N^{3/2}$  in order for the  $O(1/M)$  correction term in Eq. (D 6) to be small compared to the width of the  $\chi^2$  distribution. Therefore the standard  $\chi^2$  test is only valid if  $M = N^{3/2}$  (not true for our random lens test, with  $M = 78$  and  $N = 39$ ).